



The impact of sea bottom effects on the retrieval of water constituent concentrations from MERIS and OLCI images in shallow tidal waters supported by radiative transfer modeling



Behnaz Arabi^{a,*}, Mhd. Suhyb Salama^a, Daphne van der Wal^{a,b}, Jaime Pitarch^c, Wouter Verhoef^a

^a Faculty of Geo-Information Science and Earth Observation (ITC), Department of Water Resources (WRS), University of Twente, P.O. Box 217, 7500AE, Enschede, the Netherlands

^b NIOZ Royal Netherlands Institute for Sea Research, Department of Estuarine and Delta Systems, and Utrecht University, P.O. Box 140, 4400, AC, Yerseke, the Netherlands

^c NIOZ Royal Netherlands Institute for Sea Research, Department of Coastal Systems, and Utrecht University, PO Box 59, 1790AB Den Burg, Texel, the Netherlands

ARTICLE INFO

Keywords:

Remote sensing
Water quality monitoring
OLCI
Sentinel-3
MERIS
Optically shallow waters
Tidal waters
The Wadden Sea
Sea-bottom effect
Radiative transfer modeling
MODTRAN
2SeaColour

ABSTRACT

Many coastal waters include large areas of Optically Shallow Waters (OSWs) where the sea-bottom affects above-water observations of remote sensing reflectance (R_s [sr^{-1}]). If not treated, the effect of bottom reflectance will interfere with the correct retrieval of Water Constituent Concentrations (WCCs) from hyperspectral and multispectral remote sensing observations. To study this phenomenon in more detail, the existing semi-infinite 2SeaColour Radiative Transfer (RT) model was modified into a finite water layer model, bounded by a diffusely reflecting surface at the sea-bottom. From simulations with the new model, called Water - Sea Bottom (WSB) model, it was observed that a ratio of spectral bands in the Near-Infrared, bands 750 nm and 900 nm, is nearly insensitive to the WCCs and increases with the shallowness of the water, and therefore can be used as a robust index to detect OSWs. The newly established Near-Infrared Bottom Effect Index (NIBEI) was applied to a series of satellite observations over the Wadden Sea during high and low tidal phases. Images from the Medium Resolution Imaging Spectrometer (MERIS) and the Ocean and Land Colour Instrument (OLCI) were processed to retrieve WCCs of the study area. The results indicate that the sea-bottom effect in OSWs affects the accuracy of atmospheric correction and retrievals. On the other hand, applying the NIBEI to flag OSWs improves the reliability and consistency of WCCs maps. The application of proposed NIBEI on satellite images requires only Top Of Atmosphere (TOA) radiances at 750 nm and 900 nm and does not depend on atmospheric correction and ancillary local input data (e.g., bathymetry map, bottom type, empirical coefficients, in-situ measurements). As a result, the proposed NIBEI can readily be applied to detect OSWs on various ocean colour remote sensors in various shallow coastal regions.

1. Introduction

By the end of 2019, the world's population is expected to reach about 7.7 billion people and is projected to continue to increase to nearly 11 billion by 2100 (UN Population Division, 2019). Between 30% and 70% of this population lives within 100 km of the coastline areas (Kummu et al., 2011; UNEP, 2006; Wilson and Fischetti, 2010). Therefore sustainable monitoring, maintenance, and protection of coastal waters are vital for ensuring human/animals/ecosystem health, recreation, environmental stewardship, fisheries, and continued economic growth (Barbier, 2011; UNEP, 2006).

Continuous monitoring and conservation of biological diversity are some of the most important factors in healthy ecosystem maintenance of coastal regions (Millennium Ecosystem Assessment., 2005). In this respect, a global overview was recently provided to define the framework of water designated uses and current challenges that cross these regions in all continents by the United Nations (UN), World Health Organization (WHO), World Bank and 2018 report of Sustainable Development Goals (SDGs) (Lawford et al., 2013; IOCCG, 2012; Marmot and Bell, 2018). These frameworks describe the requirements and needs from which a significant part of them can be addressed with remote sensing of water quality in terms of measuring the core water quality

* Corresponding author.

E-mail addresses: b.arabi@utwente.nl (B. Arabi), s.salama@utwente.nl (M.S. Salama), daphne.van.der.wal@nioz.nl, d.vanderwal@utwente.nl (D. van der Wal), jaime.pitarch@nioz.nl (J. Pitarch), w.verhoef@utwente.nl (W. Verhoef).

indicators of Chlorophyll-a (Chla), Suspended Particulate Matter (SPM) and Coloured Dissolved Organic Matter (CDOM) concentrations (Brando and Dekker, 2003; Dekker, 1993; Ritchie et al., 2003; IOCCG, 2000). Monitoring spatio-temporal variation of these three Water Constituent Concentrations (WCCs) in terms of generating reliable WCC maps from satellite images, overcomes the limitations of temporal coverage and geographic extent of traditional sampling and approaches. Coupled with field-based observations, satellite remote sensing of water quality provides comprehensive and cost-effective information over highly dynamic coastal waters and is a big step of change from a station-oriented to a system-oriented monitoring approach (Ammenberg et al., 2002; Dekker, 1993; Kutser et al., 1998; Vrieling, 2006; Lepper, 2005).

In this respect, the Copernicus program (the European Union's Earth observation program coordinated and managed by the European Commission in partnership with the European Space Agency (ESA)) (<https://www.copernicus.eu/en>) launched satellites practically designed for water quality monitoring like the MEdium Resolution Imaging Spectrometer (MERIS) and the Ocean and Land Colour Imager (OLCI) on ENVISAT and Sentinel-3 platforms, respectively (Gons et al., 2002; Han et al., 2016; Mishra and Mishra, 2012; Toming et al., 2017). Having free access to these satellites' products have encouraged governmental organizations, water quality managers, private sectors, stakeholders and the scientific community to invest in satellite water quality monitoring in order to link anthropogenic stressors to water environmental responses that may impact designated uses (Doerffer et al., 1999; Kutser et al., 2006; Pitarch et al., 2019, 2016; Schroeder et al., 2007). However, satellite remote sensing of water quality in shallow coastal waters is found to be among the most challenging studies for optical remote sensing (Cannizzaro and Carder, 2006; Dekker, 1993; Kutser, 1997; Liu et al., 2003; Ritchie et al., 2003).

Recent studies have reported three main problems of i) atmospheric correction, ii) water retrieval algorithms and iii) the sea-bottom effect on optical remote sensing of shallow coastal areas (Ammenberg et al., 2002; Carpintero et al., 2015; Lee et al., 1999; Lee et al., 1994; Maritoren et al., 1994; Moore et al., 1999; Salama et al., 2012a, 2012b; Salama and Su, 2010; Volpe et al., 2011; Wang, 2005; Wang and Shi, 2007). Although many studies have addressed the problems of atmospheric correction methods and water retrieval algorithms (Hu et al., 2000; Pan et al., 2017; Salama et al., 2012a, 2012b; Salama and Shen, 2010; Siegel et al., 2000; van der Woerd and Pasterkamp, 2008; Wang, 2007), the accuracy of optical remote sensing products is still problematic due to the critical issue of the sea-bottom effect on satellite observations (Li et al., 2017, 2003; Zhao et al., 2013). Indeed, most of the water retrieval algorithms, implemented in various ocean colour remote sensors assume the upwelling water-leaving radiance is only the result of water column constituents and ignore the sea-bottom contribution into their retrievals (Gordon and Wang, 1994; Zhan et al., 2003). Consequently, the reliability of generated Chla, SPM, and CDOM concentration maps from satellite images over shallow areas will remain questionable (Ackleson, 2003; Albert and Gege, 2006; Li et al., 2003). This has a negative impact on further environmental plans and programs by decision-makers for maintenance, protection, and monitoring of many vital coastal waters (Green et al., 1996; Mumby et al., 1999). Therefore the hydro-optical algorithms should include the sea-bottom effect in order to accurately retrieve WCCs from atmospherically corrected water-leaving reflectance (Gitelson et al., 2008; Lee and Carder, 2002). The sea-bottom has a substantial influence on water leaving remote sensing reflectances (R_{rs}) recorded at the water surface level and accordingly on Top Of Atmosphere (TOA) radiances at the satellite level (Albert and Mobley, 2003; Garcia et al., 2018; Lee et al., 1998; Liu et al., 2003). R_{rs} values will be modified by light reflected from the sea-bottom, depending on local water depth, water transparency and the nature of the bottom surface in Optically Shallow Waters (OSWs) (Cannizzaro and Carder, 2006; Maritoren et al., 1994) while metrically shallow depth waters can still be classified as

"optically deep" or " optically shallow" waters. Regions with either low turbidity or shallow depth, or both, are typically characterized as OSWs, where regular water quality retrieval algorithms cannot detect WCCs accurately. The term "optically shallow" is also dependent on the wavelength of the incident light, since the effects of water column attenuation vary substantially with the total absorption coefficient, which is strongly spectrally dependent (Conger et al., 2006). This can interfere with the correct retrieval of WCCs from R_{rs} values or TOA radiances while using water retrieval algorithms (Durand, 2000; Volpe et al., 2011; Voss et al., 2003).

So far, most studies that address the application of optical remote sensing techniques to complex OSWs (Phinn et al., 2008), have focused on habitat classification or bathymetry mapping. This was commonly done by establishing statistical relationships between image-pixel values and field-measured water depths (Dierssen et al., 2003; Eugenio et al., 2015; Gao, 2009). For example, Brando and Dekker (2003) applied an integrated physics-based mapping approach to retrieve bathymetry, substratum type and WCCs using airborne hyperspectral observations at the Moreton Bay, Australia (Brando and Dekker, 2003). Their investigations suggested that the quantitative identification and screening of Optically Deep Waters (ODWs) and quasi-ODWs lead to improved precision in the depth retrievals. Hu (2009) and Hu et al. (2010) suggested the index of Floating Algae Index (FAI) to discover macro-algae and cyanobacteria in the Yellow Sea and the lake Taihu located in China from Moderate Resolution Imaging Spectroradiometer (MODIS) images (Hu, 2009; Hu et al., 2010). Their investigations showed that the FAI is sensitive to turbid waters and shallow depths. Although these studies finally helped to improve water depth and bottom type estimates from remote sensing observations, there are only a few reports to develop water retrieval algorithms in order to accurate retrieve WCCs over OSWs (Cannizzaro and Carder, 2006; Lee et al., 1999; Volpe et al., 2011). However, these algorithms require many input data, such as hyperspectral measurements, bathymetry maps, empirical coefficients, in-situ measurements, and intensive calibration/validation. As a result, these algorithms are typically site-specific and are not transferable to other locations.

One alternative, fast, and cost-effective approach to tackle the sea-bottom effect problem in coastal waters is to flag OSWs when retrieving WCCs. This can improve the reliability and consistency of satellite products of WCCs. Therefore some efforts have been made to determine very shallow areas from bathymetry maps in order to flag them while generating WCC maps (Li et al., 2017; McKinna and Werdell, 2018). However, bathymetry maps are not always available in many regions. Moreover, the sea-bottom influences remote sensing observations over these regions with either a low water column attenuation or a shallow water depth or both. For example, in a highly reflective sea-bottom type such as sand, the bottom reflectance can contribute to R_{rs} values in the blue part of the spectrum even for deep and transparent waters (Chybicki, 2017).

Furthermore, both the water depth level and turbidity are not constant and may vary in time and space with the different tidal phases (Elefeldt et al., 2014; Ma et al., 2018). Although the effect of tides on water depth can be modeled and corrected for as a factor in shallow tidal waters, performing such correction requires intensive measurements and modeling. Therefore the skills needed to apply a depth metric in discriminating ODWs from OSWs are limited, in particular for coastal areas.

The main goal of this paper is to increase the reliability and consistency of WCC satellite products in complex shallow tidal waters through proper flagging of OSWs. To achieve this goal, we conducted this research in three different phases "as: i) simulate and evaluate sea-bottom effects on above water observations using Radiative Transfer (RT) modeling, ii) define the flagging index of the Near-Infrared Bottom Effect Index (NIBEI) to distinguish OSWs and iii) implement the NIBEI on MERIS and OLCI images to improve the reliability of WCC maps".

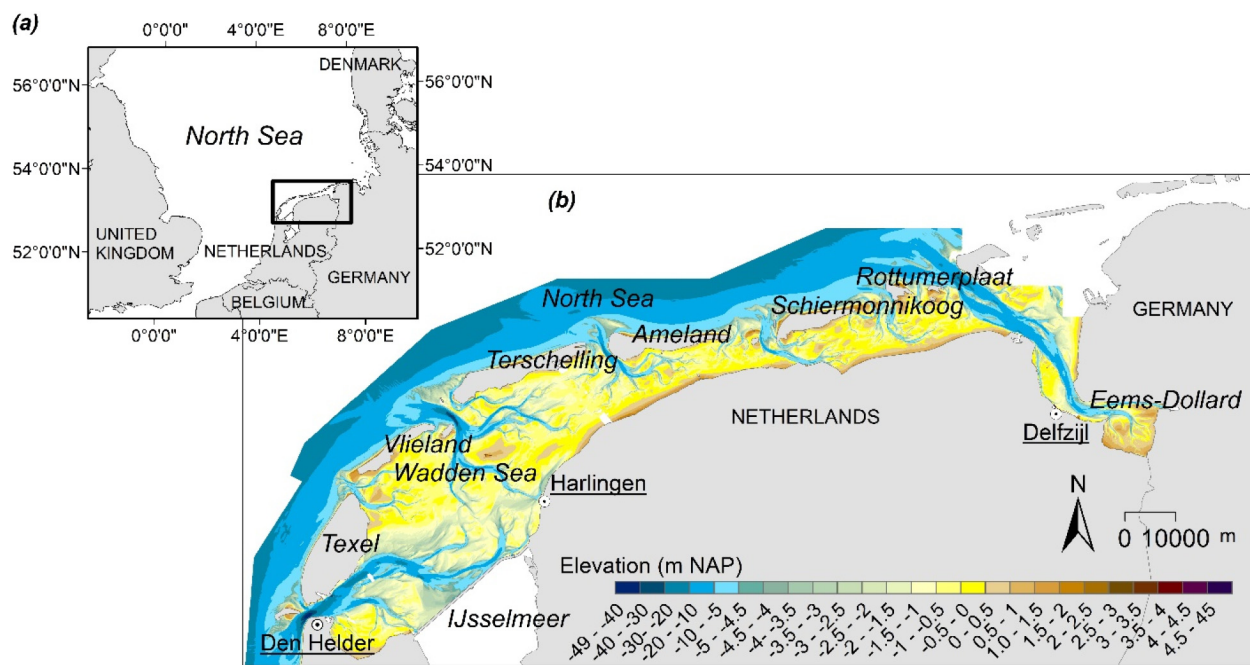


Fig. 1. (a): The geographic location of the Dutch Wadden Sea and lake IJsselmeer in Europe; (b): the elevation of the Dutch Wadden Sea showing the configuration of barrier islands, inlets, channels, shoals, and tidal flats. The elevation is relative to m Normaal Amsterdam Peil (NAP) (the Dutch ordnance datum, which is about mean sea level, and is integral to the European Vertical Reference System); elevation data are obtained from Rijkswaterstaat (2007–2012).

2. Study area

We selected the Dutch Wadden Sea as the study area of this research. The Dutch part of the Wadden Sea comprises about 66% of the whole Wadden Sea, the biggest continuous coastal and tidal area in Europe and the world. The whole Wadden Sea extends to Germany and Denmark with a total surface area of 2500 km² (Beukema, 1976). The monitoring of this region is mandatory following the European Marine Strategy launched in 2002 and its inclusion on the UNESCO World Heritage List since July 2009 (Hommersom, 2010). The Dutch Wadden Sea is a home and a wintering place for up to twelve million birds each year (Boere and Piersma, 2012). Fig. 1 illustrates the geographic location and elevation of this area.

The channels in the Dutch Wadden Sea are typically deeper than +10 m, while the tidal flats are typically up to +1 m NAP high (Fig. 1). The Dutch Wadden Sea experiences a semi-diurnal tidal regime, with the tidal range increasing from West to East. The mean tidal range at tide gauge station Harlingen (Fig. 1(b)) is +1.94 m (Rijkswaterstaat, 2018). Thus, water depths are less than a few meters in most parts of the Dutch Wadden Sea.

The reason to select the Dutch Wadden Sea as the study area of this research was its limited water depth, combined with tidal variations. The tides produce a strong mixing of the water constituents (Cadée, 1986; Postma, 1982). Accordingly, the extent of OSWs varies with the different tidal phases, which complicates the task for remote sensing scientists and water quality managers to generate reliable WCC maps. This area could be considered as a good example for optical remote sensing of water quality in complex waters. Due to the shallowness of the water, tidal variation, variable concentration of water constituents, and the occurrence of many rainy and cloudy days, satellite remote sensing of water quality has remained problematic in this region (Hommersom, 2010; Cadée and Hegeman, 2002; Garaba et al., 2014; Giesen et al., 1990; Hommersom et al., 2010a; Hommersom et al., 2010b; Philippart et al., 2013; Reuter et al., 2009; Salama et al., 2009; Tillmann et al., 2000).

3. Dataset

In this study, we used satellite images of the MERIS and Ocean and Land Colour Instrument (OLCI). These sensors are mainly designed for water quality monitoring in open oceans and open coastal areas (Ambarwulan et al., 2011; Ambarwulan et al., 2012; Harvey et al., 2014) while they are likely the optimal past and present sensors for near real-time frequent monitoring applications for spatially constrained inland and coastal waters (Matthews et al., 2012).

The MERIS was one of the instruments on board of the ENVISAT mission and monitored the Earth between 30th of April 2002 and 9th of May 2012. The high sensitivity and extensive dynamic range of the MERIS sensor (full spatial resolution: 300 m) have been widely used for ocean, lakes, and coastal water remote sensing studies (Majozi et al., 2014; Odermatt et al., 2012; Pasterkamp et al., 2003). The MERIS sensor covered the Dutch Wadden Sea at around 12:30 p.m. (Central European Summer Time (CEST)) every three days, with 15 bands covering the spectral ranges from 400 nm to 950 nm. The MERIS sensor stopped functioning in May 2012 and was continued by the OLCI on board of the Sentinel-3 A and B satellites since 2016 and 2018, respectively (Saulquin et al., 2016). The OLCI is an improved successor of the MERIS sensor with higher accuracy, greater wavelength, and coverage (Hieronymi et al., 2017). It has the same spectral bands as the MERIS, plus six extra bands at 400 nm, 673.75 nm, 764.37 nm, 767.5 nm, 940 nm, and 1020 nm. The OLCI sensor (full spatial resolution: 300 m) has a revisit time of two-three days on average at around 12:00 pm (CEST) over the Dutch Wadden Sea. An overview of the MERIS and OLCI bands is presented in Table 1.

The MERIS and OLCI images of this research were provided by ESA (<https://www.esa.int/ESA>) within the framework of the Integrated Network for Product. We used the Sentinel Application Platform image processor SNAP (version 6.0) and the image analysis software of ENVI (version 5.5) to process MERIS and OLCI images in this research.

4. Methodologies

Fig. 2 summarizes the methodology of this research.

Table 1
The MERIS and OLCI spectral band configurations.

Band number/sensor	Band center (nm)		Band width (nm)	
	MERIS	OLCI	MERIS	OLCI
1	412.5	400	10	15
2	442.5	412.5	10	10
3	490	442.5	10	10
4	510	490	10	10
5	560	510	10	10
6	620	560	10	10
7	665	620	10	10
8	681.25	665	7.5	10
9	708.75	673.75	10	7.5
10	753.75	681.25	7.5	7.5
11	761.87	708.75	2.5	10
12	778.75	753.75	15	7.5
13	865	761.25	20	2.5
14	885	764.37	10	7.5
15	900	767.5	10	2.5
16	–	778.75	–	15
17	–	865	–	20
18	–	885	–	10
19	–	900	–	10
20	–	940	–	20
21	–	1020	–	40

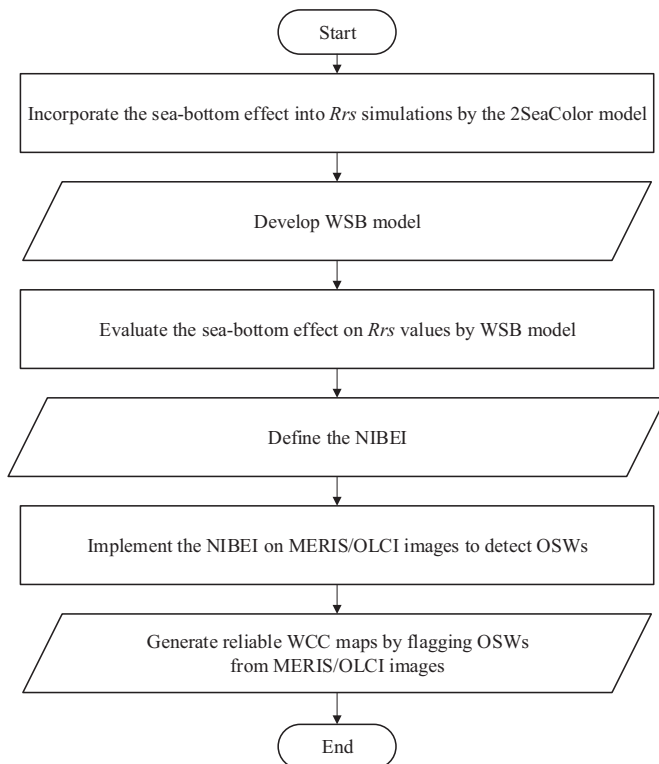


Fig. 2. The diagram of the implemented methodology in this research.

4.1. The Water - Sea Bottom (WSB) model

The performance of two-stream Radiative Transfer (RT) modeling of 2SeaColour (Salama and Verhoef, 2015) in optical remote sensing of tide-affected and turbid coastal waters has been demonstrated in previous studies (Arabi et al., 2018; Arabi et al., 2016; Salama and Verhoef, 2015; Yu et al., 2016a, 2016b). In their most recent effort, Arabi et al. (2018) showed that the 2SeaColour model is capable of accurately retrieving WCC concentrations from in-situ hyperspectral measurements collected under different conditions of dates, Solar Zenith Angles (SZAs) and water turbidities in ODWs of the Dutch Wadden Sea. They

considered the simultaneous contribution of Chla [mg m^{-3}], SPM [g m^{-3}], and CDOM absorption at 440 nm [m^{-1}] concentrations on simulated R_{rs} values by the 2SeaColour model. However, in their research, the effect of the sea-bottom was not considered in simulating R_{rs} values due to the moderate depth of the NIOZ jetty station (the NJS) which is located on the Southern tip of the island of Texel (water depth $> 5 \text{ m}$) (Arabi et al., 2018).

In this study, we extended the 2SeaColour model by incorporating the sea-bottom effect. The R_{rs} values are modeled as a function of five independent variables, namely Chla, SPM, CDOM, bottom albedo (ba), and water depth (wd). The improved model, called Water - Sea Bottom (WSB), was used to evaluate the sensitivity of R_{rs} values to the sea-bottom effect in different parts of the spectrum in order to define the NIBEI as described in the following paragraphs.

The 2SeaColour model is based on a two-stream approach, first proposed by Duntley (1942), with direct solar radiation included as a source of incident flux. The model predicts the Directional-Hemispheric Reflectance Factor (DHRF) of a semi-infinite water layer as:

$$r_{sd}^{\infty} = \frac{\sqrt{1+2x} - 1}{\sqrt{1+2x} + 2\mu_w} \quad (1a)$$

where x is the ratio of the backscattering to the absorption coefficient ($x = b_b/a$), and μ_w is the cosine of the SZA beneath the water surface. The reflectance factor r_{sd}^{∞} can be approximated by $Q \times R(0^-)$ in sunny situations, where $Q = 3.25$ and $R(0^-)$ is the irradiance reflectance value below the water surface (Morel and Gentili, 1993). The model also gives the reflectance for diffuse incident light, called the bi-hemispheric reflectance factor or BHRF, which is given by

$$r_{dd}^{\infty} = \frac{\sqrt{1+2x} - 1}{\sqrt{1+2x} + 1} \quad (1b)$$

If sunlight dominates over the diffuse incident flux from the sky, only Eq. (1a) is applied in practice. In the extensive literature on two-stream approximations of RT, particularly in Duntley (1942), one can find quite different expressions for these reflectance factors, but the ones presented above are particularly suitable for model inversion purposes since x can be derived easily from the reflectances. Derivations of Eqs. (1a)–(1b) are given in Appendix A. For more details on the 2SeaColour model, readers are referred to Salama and Verhoef (2015).

To incorporate the sea-bottom effect in the 2SeaColour model, the semi-infinite water layer was replaced by a finite layer of given metrical depth d , and the number of model outputs was extended with extra reflectance and transmittance factors that enable calculating the effect of a sea-bottom with a given Lambertian reflectance r_b on R_{rs} values. The assumption here is that the sea-bottom resembles a Lambertian surface. In Verhoef (1985), the adding equations for calculating the reflectance of the combination of a turbid medium layer and a background surface with a reflectance r_b were given by Eqs. (26a)–(b), which were slightly adapted here for a Lambertian background:

$$r_{dd} = \rho_{dd} + \frac{\tau_{dd} r_b \tau_{dd}}{1 - r_b \rho_{dd}} \quad (2)$$

$$r_{sd} = \rho_{sd} + \frac{(\tau_{ss} + \tau_{sd}) r_b \tau_{dd}}{1 - r_b \rho_{dd}} \quad (3)$$

where the double subscripts indicate the types of flux on incidence and exit, respectively, and s stands for direct solar flux and d for semi-isotropic diffuse flux. Reflectances caused by volume scattering inside the layer have the symbol ρ , and transmittances have the symbol τ . The direct transmittance for sunlight is τ_{ss} . The resulting DHRF of the combination water - bottom is called r_{sd} , and the Bi-Hemispherical Reflectance Factor (BHRF) is r_{dd} .

To generate input spectra of the bottom reflectance, a sub-model called Brightness-Shape-Moisture (BSM) is applied. This model is based on the statistical Global Soil Vectors (GSVs) approach of Chongya and Hongliang (2012) and was more recently also used by Verhoef et al.

(2018). This also implies that vegetated sea-bottoms are not yet considered in the current approach. Unvegetated sandy and muddy bottoms are the most common sea-bottom types in the Dutch Wadden Sea. Particularly on tidal flats, benthic micro-algae (e.g., diatoms) may be present, while at limited places, macroalgae are growing (van der Wal et al., 2010). Like vascular plants, these absorb part of the visible light, particularly in red wavelengths, but unlike higher plants and macroalgae, benthic diatoms do not show increased reflectance in the near-infrared (Kromkamp et al., 2006; van der Wal et al., 2010). The BSM model has four input variables, dry soil brightness, two spectral shape variables, and the volumetric soil moisture percentage. In this particular application, only the dry soil brightness variable was varied to generate spectra of constant shape. Dry soil brightness in this context is formally defined as the square root of the sum of the three squared weight coefficients applied to the basis spectra to fit a given dry soil spectrum. Changing soil brightness affects the whole soil spectrum proportionally, while the spectral shape is preserved. The so-called irradiance reflectance just beneath the water surface is:

$$R(0^-) = \frac{r_{sd}E_s(0) + r_{dd}E_d^-(0)}{E_s(0) + E_d^-(0)} \quad (4)$$

where $E_s(0)$ and $E_d^-(0)$ are the direct solar irradiance and the diffuse downward irradiance incident at the top of the water layer, respectively. To include the effect of the water-air interface, we finally estimate R_{rs} by Mobley (2003):

$$R_{rs} = \frac{0.52R(0^-)}{Q - 1.7R(0^-)} \quad (5)$$

In the turbid medium scattering model for the water layer, a similarity transform (van de Hulst, 1980) is applied in such a way that all forward scattering greater than the backscatter coefficient is ignored, so that effectively isotropic scattering results. Accordingly, the beam extinction coefficient c in m^{-1} was reduced to:

$$c = a + 2b_b \quad (6)$$

where a is the absorption coefficient and b_b the backscattering coefficient. This means that the forward scattering peak due to Mie scattering by particles in the water is ignored and treated as the light that is not scattered at all. The transformed single scattering albedo ω is given by:

$$\omega = 2b_b/c = \frac{2b_b}{a + 2b_b} \quad (7)$$

The similarity transform, effectively resulting in an anisotropic scattering approximation, simplifies the description of RT in the layer in the matrix-vector form to:

$$\frac{d}{dz} \begin{pmatrix} E_s \\ E^- \\ E^+ \end{pmatrix} = \begin{pmatrix} k & 0 & 0 \\ -s' & \alpha & -\sigma \\ s & \sigma & -\alpha \end{pmatrix} \begin{pmatrix} E_s \\ E^- \\ E^+ \end{pmatrix} = \begin{pmatrix} k & 0 & 0 \\ -1/2\omega k & \kappa - \omega & -\omega \\ 1/2\omega k & \omega & -(\kappa - \omega) \end{pmatrix} \begin{pmatrix} E_s \\ E^- \\ E^+ \end{pmatrix} \quad (8)$$

where z is the metrical depth, E_s is the direct solar flux, E^- is the downward diffuse flux, E^+ is the upward diffuse flux, k is the extinction coefficient for direct sunlight, and κ is the one for diffuse light. The extinction coefficients for diffuse and direct light are given by $\kappa = 2$, and $k = 1/\mu_w$, respectively, where μ_w is the cosine of the underwater SZA. A generic solution to Eq. (8) can be formulated in matrix-vector form by:

$$\begin{pmatrix} E_s(b) \\ E^-(b) \\ E^+(t) \end{pmatrix} = \begin{pmatrix} \tau_{ss} & 0 & 0 \\ \tau_{sd} & \tau_{dd} & \rho_{dd} \\ \rho_{sd} & \rho_{dd} & \tau_{dd} \end{pmatrix} \begin{pmatrix} E_s(t) \\ E^-(t) \\ E^+(b) \end{pmatrix} \quad (9)$$

where (b) and (t) stand for the bottom and the top of the layer, respectively. The direct transmittance of the layer is given by $\tau_{ss} = \exp(-kcd)$, where d is the metrical thickness of the water layer. The other

Table 2

The variables, units, and their corresponding values for simulations of R_{rs} spectra using the WSB model.

Variable	Unit	Values
Chla concentration	[mg m ⁻³]	0 100
SPM concentration	[g m ⁻³]	0 50
CDOM absorption	[m ⁻¹]	0
Bottom albedo		0.1 0.3 0.5
Water depth	[m]	0.05 .1 .2 .4 .6 .8 1 1.2 1.4 1.6 2 5 20 50

reflectance and transmittance quantities are given in Appendix A.

We conducted a series of simulations with the developed WSB model to investigate the sea-bottom effect on the R_{rs} spectra at the sea surface level. The used values of the variables in the R_{rs} simulations by the WSB model are presented in Table 2. It should be mentioned that the same Inherent Optical Properties (IOPs) model's parametrizations, as listed in Arabi et al. (2018), were used to calculate total absorption (a) and backscattering (b_b) coefficients of WCCs, and accordingly to simulate R_{rs} spectra in this study.

As can be seen in Table 2, the effect of CDOM absorption at 440 nm [m⁻¹] is considered negligible in this study. The reason is that CDOM absorption at 440 nm [m⁻¹] has only a significant effect on the blue region of the spectrum. As a result, it can reduce the blue colour of otherwise clear and deep waters. In other spectral regions, the effects are quite limited compared to those of Chla [mg m⁻³] and SPM [g m⁻³]. Therefore, the variation in CDOM absorption at 440 nm [m⁻¹] was ignored in the simulations.

The resulting R_{rs} spectra using the WSB model are presented on a logarithmic scale in Fig. 3.

From Fig. 3, it is obvious that all parts of the R_{rs} spectrum can be affected by light reflected by the sea-bottom, depending on the water column attenuation. For absolutely pure water (i.e., pure freshwater free from salinity), the influence of the bottom albedo (in the blue-green parts of the spectrum) remains noticeable for water depths up to 50 m. However, in the NIR (wavelengths > 750 nm), the R_{rs} spectra are unaffected by the bottom albedo for water depths > 2 m. There, the shape of the spectrum is completely determined by the absorption of water itself (Ruddick et al., 2006), although the magnitude of the spectrum is still dependent on the scattering due to the Chla and SPM concentrations together. Plotted logarithmically, this gives a series of spectra that are shifted parallel in the vertical direction. For absolutely pure water with a depth > 2 m, the slope of the spectrum between 750 nm and 900 nm is slightly larger than for turbid waters, but other simulations (not shown here) revealed that for low concentrations of Chla or SPM the spectral shape was practically the same as for high concentrations. Thus, with the exception of pure water, spectral shapes in this region are nearly invariant, regardless of WCCs. This phenomenon was termed "similarity spectrum" by Ruddick et al. (2006), and normalization of NIR spectra by the reflectance at one wavelength (e.g., 750 nm) gives nearly a single normalized spectrum that is independent of WCCs.

From the investigation of the WSB model's R_{rs} simulations, we defined the NIBEI to detect the contaminated remote sensing observations by the sea-bottom effect using R_{rs} values at water surface level and TOA radiances at satellite level as explained in Sections 4.2 and 4.3, respectively.

4.2. Define the NIBEI

From the simulations presented in Fig. 3, it was found that for water depths < 2 m, the R_{rs} spectral shapes start deviating from the ones for water depths > 2 m. Therefore, by detecting deviations from the expected similarity R_{rs} spectrum, OSWs can be discriminated from ODWs. The obvious candidate index for this concept is the ratio of the R_{rs} values at 750 nm and 900 nm, which measures the spectral slope over

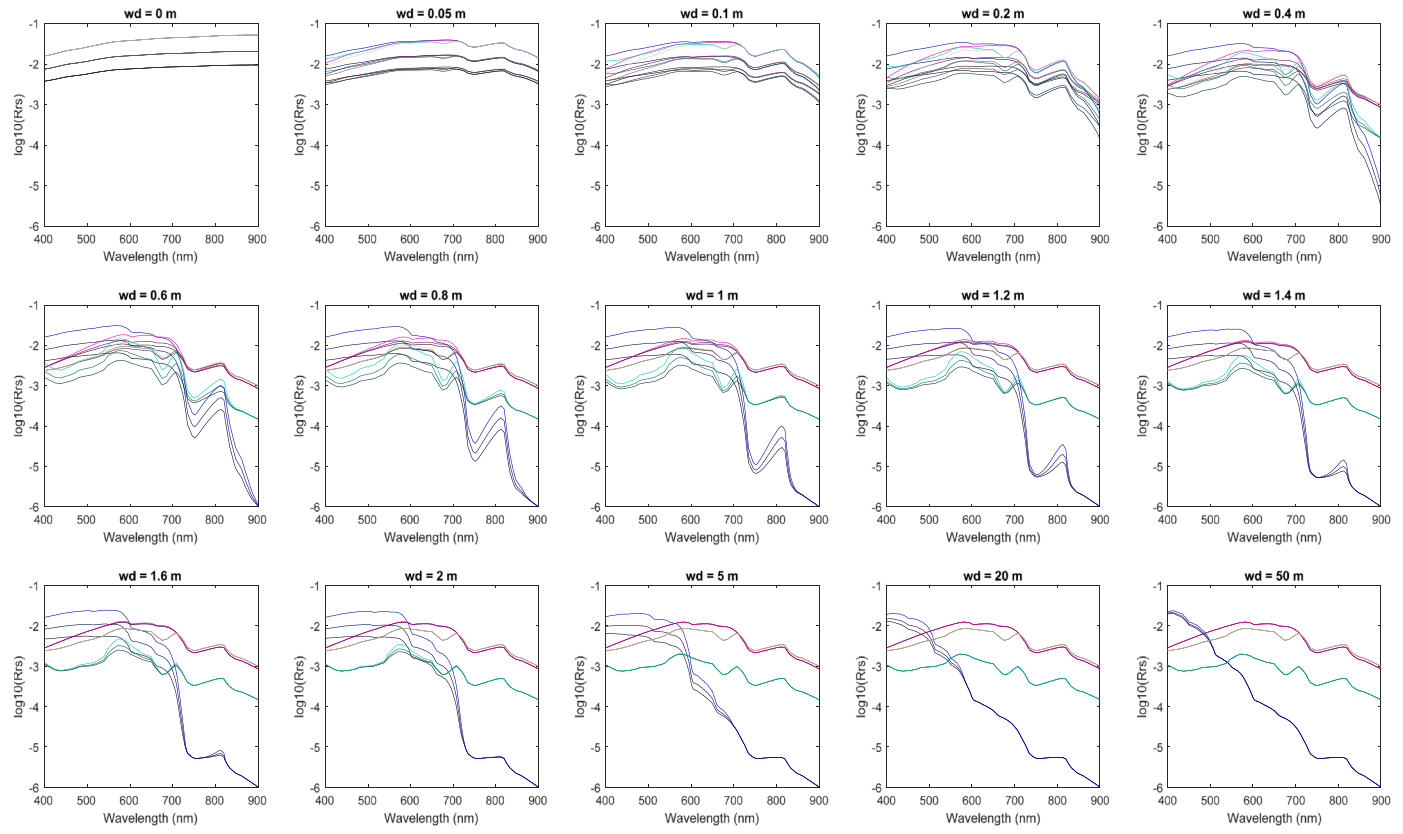


Fig. 3. Spectra of $^{10}\log(R_{rs})$ generated by the WSB model for fifteen water depths (wd), three bottom albedos (ba), two concentrations of Chla [mg m^{-3}], and two of SPM [g m^{-3}] including absolutely pure water. Water depth (wd) is indicated above each graph: absolutely pure water in blue, high Chla in green, high SPM in red, both high in yellow. Line brightness modulated by bottom albedo. (For interpretation of the references to color in this figure legend, the reader is referred to the web version of this article.)

this interval. As was found from inspection of Fig. 3, this ratio value ($R_{rs}[750 \text{ nm}]/R_{rs}[900 \text{ nm}]$) is constant for water depths $> 2 \text{ m}$. However, starting at water depths between 2 m and 0.4 m , the ratio value first increases sharply reaching a maximum value at a water depth of about 0.4 m , then finally declining again for shallower, towards its level for a dry bottom. The sharp increase of the ratio value is caused by a rising R_{rs} value due to the bottom effect beginning at 750 nm , while at 900 nm , the water layer is still optically deep due to the higher water absorption coefficient there.

The reason why a NIBEI is useful is that at both wavelengths 750 nm and 900 nm , the absorption coefficient of pure water is high enough to ensure that the optically deep stage is reached well below 5 m deep, probably already below 2 m deep, whether the water is turbid or not. For optically deep waters, R_{rs} values are determined by the ratio b_b/a . In the NIR, b_b will vary little with wavelength if some turbid material is present. Not much turbidity is needed for that since the b_b of pure water is very small in the NIR, so it will soon be overwhelmed by the b_b of sediments or other particles. Therefore, for water containing a little turbid material, one may assume that in ODWs, R_{rs} , and therefore the ratio $750 \text{ nm}/900 \text{ nm}$ is only determined by the pure water absorption. Since this ratio is well above unity, it is clear that at 900 nm the absorption by water is substantially stronger than at 750 nm . This also means that the sea-bottom effect will first become visible at 750 nm . The effect will always be an increase of R_{rs} values since the sea bottom will start contributing to the R_{rs} values by the upward transmission of solar radiation reflected by the sea bottom. The same effect will finally happen at 900 nm but at a shallower depth. Thus, with increasing shallowness, the ratio will first go up then come down again since the bottom effect has become important at both wavelengths. Sea-bottoms usually have a nearly flat or slightly increasing reflectance spectrum in

the NIR. This holds not only for sandy and muddy bottoms but also for sea-bottoms with benthic diatoms (and even macro-algae) since we are looking only at NIR wavelengths.

The NIBEI ratio has a constant value of 2.67 using R_{rs} values for ODWs. This follows from the approximation of $R_{rs}[750 \text{ nm}]/R_{rs}[900 \text{ nm}] \sim a_w[900 \text{ nm}]/a_w[750 \text{ nm}]$. Therefore this threshold can be easily used to discriminate OSWs from ODWs for the atmospherically corrected satellite images over shallow coastal waters.

4.3. Apply the NIBEI on MERIS/OLCI images to discriminate OSWs from ODWs

An application of the NIBEI is due to its capability to detect OSWs from image-pixel TOA radiances on satellite images. The reason is that by defining the NIBEI based on TOA radiances, there is no need to have information about atmospheric properties (i.e., visibility and aerosol type) or to remove the atmospheric effect and calculate R_{rs} values from TOA radiances. This not only speeds up the process of detecting OSWs from Earth Observation (EO) data but also increases the reliability of the approach since doing an accurate atmospheric correction method is the most problematic step of satellite remote sensing of coastal waters. As a result, applying inappropriate atmospheric corrections can easily lead to having inaccurate R_{rs} estimates, which negatively affects the performance of the NIBEI.

Considering the simulations of Fig. 3, in a generated NIBEI map from satellite images (i.e., each pixel value is equal to band-center [750 nm]/band-centre[900 nm]), OSWs will show maximum values compared to ODWs, whether one uses images of R_{rs} or TOA radiances, since atmospheric effects in the NIR are only moderate. Moreover, OSWs will look brighter than ODWs regardless of atmospheric effects.

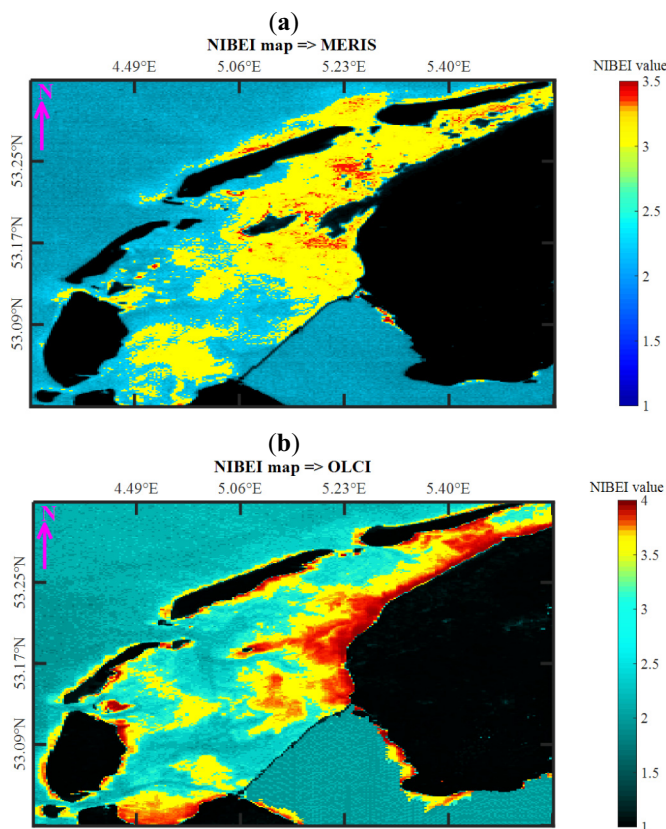


Fig. 4. The generated maps of the NIBEI values over the study area from; (a) the MERIS image captured on 25-03-2012, the NIBEI threshold = 3; (b) the OLCI image captured on 01-07-2018 the NIBEI threshold = 3.5.

Therefore, there will be considerable differences in the NIBEI values as well as image-pixel colours between OSWs and ODWs in a NIBEI map.

Fig. 4 shows two examples of the NIBEI maps generated from MERIS and OLCI images, separately, using Matlab 2016b programming (the multi-paradigm numerical computing environment and proprietary programming language developed by MathWorks [<https://www.mathworks.com/products/matlab.html>]). The pixel-NIBEI values in these maps were defined for MERIS and OLCI sensors, separately, as described in Table 3:

As can be seen from the legends of Fig. 4(a) and (b), there is high spatial variability in the NIBEI values and image colours in different parts of each map. Following the simulations of Fig. 3, pixels with brighter colours and higher NIBEI values are classified OSWs and pixels with darker colours, and lower NIBEI values are ODWs. These results are also in agreement with the bathymetry of the study (Fig. 1). In both maps, the North Sea waters, some internal channels of the Dutch Wadden Sea and the IJsselmeer lake show darker colours (displayed in dark blue/green) with much lower NIBEI values (Fig. 4(a): NIBEI values < 3; Fig. 4(b): NIBEI values < 3.5) in comparison to the rest of the region. The bathymetry of the study area (Fig. 1) is the evidence that these regions have such high water levels (water depth > 15 m) that the sea-bottom effect can not influence the recorded observations and therefore are ODWs. On the other hand, there are regions, mainly

nearby the Wadden Sea coast as well as south of the barrier islands, which show brighter colours (displayed in yellow/red) with considerable increases in the NIBEI values (Fig. 4(a): NIBEI values > 3; Fig. 4(b): NIBEI values > 3.5). These regions can be detected as OSWs by considering the bathymetry of the study area (Fig. 1) as these regions have very low water level (water depth < 1.5 m) with a very high risk of a sea-bottom contribution to remote sensing observations. The mainland coast, Wadden islands, and exposed tidal flats are classified as land in the preprocessing (black areas in Fig. 4); a small strip fringing these areas have low NIBEI values, indicating areas with dry sea-bottom (e.g., in Fig. 4(a)).

From this investigation, it can be concluded that OSWs can be distinguished from ODWs in MERIS and OLCI images by applying the NIBEI to TOA radiances. However, first, a NIBEI threshold should be determined per image, separately. The NIBEI threshold has a value for each image. For example, in Fig. 4(a) and (b) the NIBEI thresholds are 3 and 3.5 for MERIS and OLCI images, respectively. However, as was shown in Fig. 4, these thresholds can be easily determined by having a quick visual image-based inspection per satellite image.

The reason for multi NIBEI thresholds is that these thresholds are based on TOA radiances. The recorded TOA radiances at satellite image-pixels are a function of atmospheric path radiance, the total gain factor, the spherical albedo, and water-leaving reflectances by using Eq. (10) (Verhoef and Bach, 2003):

$$L_{TOA} = L_0 + \frac{Gr}{1 - Sr} \quad (10)$$

where L_{TOA} is the TOA radiance value [$\text{W m}^{-2} \text{ sr}^{-1} \mu\text{m}^{-1}$], r is the hemispherical water-leaving remote sensing reflectance ($=\pi R_{rs}$). L_0 , G , and S are the atmospheric parameters atmospheric path radiance, the total gain factor, and the spherical albedo, respectively. These parameters can be calculated by using the MODerate resolution atmospheric TRANsmision (MODTRAN) code (Berk et al., 2011). As explained by Arabi et al. (2016), the atmospheric parameters of L_0 , G , and S are a factor "of: (i) atmospheric properties in the form of visibility and aerosol type; (ii) environmental variables in the form of concentrations of ozone (O_3) and carbon dioxide (CO_2); and (iii) the illumination-observation geometry in the form of SZA, Viewing Zenith Angle (VZA) and Relative Azimuth Angle (RAA)". Therefore, it is logical that the recorded TOA radiances will be influenced by the above-mentioned factors and will not have the same values on the constant regions of a study site for images captured by different sensors on different dates, water turbidity, and atmospheric conditions. That is why, in practice, it is not possible to propose a constant NIBEI threshold to detect OSWs using TOA radiances. However, further investigations showed that the NIBEI thresholds are within a constant range and slightly differ for different sensors and images. Table 4 presents the ranges of the NIBEI thresholds for MERIS and OLCI images. These ranges are obtained by finding NIBEI thresholds from the full archive of cloud-free MERIS and OLCI images provided by ESA since 2002 till present captured under different illumination-observation geometry, water turbidity, environmental variables and atmospheric conditions using Matlab programming (Table 5).

As Table 4 shows, the NIBEI thresholds at the TOA level have a constant range (2.6–4.9) for different MERIS and OLCI images captured under different conditions.

Table 3
The NIBEI formula for satellite images.

Satellite	Band center at 750 nm	Band center at 900 nm	NIBEI for satellite images ^a
MERIS	Band-10	Band-15	Radiance [band-10]/Radiance [band-15]
OLCI	Band-12	Band-19	Radiance [band-12]/Radiance [band-19]

^a The NIBEI formula = the ratio of TOA radiances at spectral bands of 750 nm/900 nm.

Table 4

The range of the NIBEI thresholds for the full archive of MERIS and OLCI images since 2002 till present.

Satellite image	The NIBEI value in NIBEI map	The range of NIBEI thresholds
MERIS	Radiance [band-10]/Radiance [band-15]	2.6–4.6
OLCI	Radiance [band-12]/Radiance [band-19]	2.7–4.9

4.4. Application of the NIBEI

4.4.1. Generating OSW and ODW maps from MERIS/OLCI images

We tested the application of the NIBEI to generate optically shallow/deep water maps over shallow tidal waters of the Dutch Wadden Sea, where both water depths and turbidity vary corresponding to the tidal phase. To do this, we generated such maps using two MERIS and OLCI images captured during high and low tidal phases over the Dutch Wadden Sea, respectively. The image characteristics are provided in [Table 6](#).

To produce these maps, first, we generated an NIBEI map using the NIBEI formula as was described in [Section 4.3](#) and determined the NIBEI threshold per each image, separately. Next, we presented optically shallow/deep waters discriminated by the NIBEI threshold in two different colours using Matlab. The maps from these four images are presented in [Section 5.1](#).

4.4.2. Improving the reliability of WCC-retrievals from satellite images over shallow tidal waters

We tested the application of the NIBEI as an intermediate approach to flag OSWs in order to increase the reliability of satellite WCCs-maps. To do this, we compared the performance of the coupled RT atmosphere-hydro-optical model of MOD2SEA proposed by [Arabi et al. \(2016\)](#) over discriminated OSWs and ODWs by NIBEI on the same MERIS and OLCI images described in [Table 6](#).

The reason we selected the coupled MOD2SEA model was that this model is a TOA method that simulates TOA radiances in a pixel-by-pixel approach. Therefore, implementing MOD2SEA on satellite images provides the opportunity to validate the agreement of the simulated TOA radiances against the observed ones over optically shallow and deep water pixels, separately, since a dense network of in-situ measurements is not available for this area. As a result, by implementing the MOD2SEA model in this study, we were able to compare the spatial variation in spectral residual errors of TOA radiances (i.e., the Root Mean Square Error (RMSE) between the observed and the simulated TOA radiance) over OSWs and ODWs, separately. The result of this evaluation is presented in [Fig. 6](#).

The coupled MOD2SEA model uses a Look-Up-Tables (LUTs) approach that combines the modeled R_s LUTs by 2SeaColour ([Salama and Verhoef, 2015](#)) with the modeled L_0 , G, and S LUTs by MODTRAN ([Berk et al., 2011](#)) to simulated TOA radiances using Eq. (10) ([Arabi et al., 2016](#)). [Tables 7 and 8](#) present the input variables used in the MOD2SEA model to build up the LUTs of the TOA radiances.

In this study, the MOD2SEA-TOA radiances were simulated corresponding to the illumination-observation geometry and environmental

variables of each image, separately. The spectral values of simulated TOA radiances are then found by spectrally fitting the LUTs of MOD2SEA-simulated TOA radiances (using RMSE) to the actual image-pixel TOA radiances recorded at the satellite image in a pixel-by-pixel approach. For more detailed information about the MOD2SEA model, readers are referred to [Arabi et al. \(2016\)](#). Next, the spectral agreement between the simulated MOD2SEA-TOA radiances was validated against the observed ones over detected optically shallow and deep waters by the NIBEI for MERIS and OLCI images using statistical analysis. The coefficient of determination (R^2), RMSE, the Normalized Root Means Square Error (i.e., $NRMSE = RMSE/range$), and the Relative Root Means Square Error (i.e., $RRMSE = RMSE/mean$) were used for this statistical analysis. The results of this evaluation are presented in [Fig. 7](#), and the related error statistics are presented in [Tables 10, 11, 12, and 13](#).

4.4.2.1. Generating Chla, SPM and CDOM maps over the masked OSWs of the Dutch Wadden Sea.

We generated simultaneous maps of Chla concentrations [mg m^{-3}], SPM concentration [g m^{-3}], and CDOM absorption at 440 nm [m^{-1}] from the MERIS and OLCI images listed in [Table 6](#), by applying the NIBEI over the masked OSWs of the Dutch Wadden Sea. We used the MOD2SEA model to generate these WCC-retrieval maps ([Arabi et al., 2016](#)).

The simultaneous retrieval of WCCs and atmospheric properties was performed by spectrally fitting of the simulated TOA radiances (using RMSE) to observed TOA radiances for all bands except for bands 11 and 13 for the MERIS and OLCI images, respectively. These bands are located in the O_2 -A absorption region and could give erroneous results due to spectral sampling errors of MERIS and OLCI sensors ([Arabi et al., 2016](#)). Moreover, to speed up the computation and limit the combined LUT size, for every pixel and aerosol type, only five visibilities were selected from the atmospheric LUT. These visibilities were chosen to be the first five less than the minimum required visibility for which the modeled L_0 was less than or equal to the measured TOA radiance in all bands. This approach is equivalent to assuming only non-negative reflectances. Nonetheless, it dramatically increased the speed of computation while applying MatLabR2017B on a personal PC [Processor: Intel (R) Core (TM) i7 - 4700 MQ, CPU: 2.40 GHz, RAM: 7.88 GB]. Overall, the average number of pixels for each satellite image was equal to 80,000, while the land-mask would represent 39% of the whole scene. The total number of LUT cases per pixel was equal to 15 times [5 (visibility) \times 3 (aerosol types) = 15 times]. Moreover, the number of water cases in total was equal to 1764: [21 (Chla concentration [mg m^{-3}]) \times 21 (SPM concentration [g m^{-3}]) \times 4 (CDOM absorption at 440 nm [m^{-1}])] = 1764 cases]. Each image was generated in the

Table 5

The atmospheric properties, environmental variables, and illumination observation-geometry for the full archive of MERIS and OLCI images since 2002 till present.

Satellite image	Aerosol ^a type	Visibility ^b [km]	CO_2 ^c [ppm]	O_3 [DU]	SZA ^d [degree]	VZA [degree]	RAA [degree]
MERIS	M, U, R	5–100	372–396	220–480	30–60	5–30	35–150
OLCI	M, U, R	5–100	402–406	240–500	30–50	7–55	30–100

^a The capital letters of M, U, and R are representatives of aerosol types of Maritime, Urban, and Rural, respectively.

^b The atmospheric properties information can be found using available AERONET stations nearby the study site ([Zibordi et al., 2010](#)).

^c The estimates of environmental variables can be obtained from the Global Reference Networks considering the date, time, and geographic location of the study site.

^d The values of illumination-observation geometry can be directly extracted from MERIS and OLCI images using different satellite software (e.g., SNAP, ENVI, BEAM).

Table 6

Image characteristics, tidal phases, and the NIBEI thresholds.

Satellite sensor	date and time	SZA	Den Helder water level, m NAP ^a	Harlingen water level, m NAP	Delfzijl water level, m NAP	NIBEI threshold ^b
MERIS (high tide)	23-04-2010, 10h51 UTC	41°	+0.60 m incoming, at 11h50 MET	+0.12 m incoming, at 11 h50 MET	+1.19 m incoming, at 11 h50 MET	> 2.8
MERIS (low tide)	25-04-2011, 10h42 UTC	40°	+0.48 m incoming, at 11h40 MET	-0.76 m incoming, at 11 h40 MET	-1.40 m low water, at 11 h40 MET	> 2.9
OLCI (high tide)	06-06-2018, 09h51 UTC	41°	+0.60 m outgoing, at 10h50 MET	+0.34 m incoming, at 10 h50 MET	-0.95 m incoming, at 10 h50 MET	> 3.3
OLCI (low tide)	06-08-2018, 10h06 UTC	39°	+0.32 m incoming, at 11h10 MET	-1.05 m incoming, at 11h10 MET	-1.46 m outgoing, at 11h10 MET	> 3.2

^a Water level data obtained from Rijkswaterstaat (<https://waterinfo.rws.nl>), see station locations in Fig. 1. See the explanation of NAP in caption Fig. 1.^b The NIBEI threshold is estimated using the NIBEI values at the band-centre[750 nm]/band-centre[900 nm].**Table 7**The used ranges and units of WCCs in the R_{rs} LUTs by the 2SeaColour model.

Variable	Unit	Values ^a	Step ^b
Chla concentration	[mg m ⁻³]	0–100	5
SPM concentration	[g m ⁻³]	0–100	5
CDOM absorption	[m ⁻¹]	0–2	0.5

^a The range of WCC concentrations was determined based on previous studies (Hommersom, 2010).^b The CDOM absorption at 440 nm [m⁻¹] values of [0], [0.5], [1], [1.5], and [2] were used in R_{rs} LUTs.**Table 8**

The used visibility range [km] and aerosol types in atmospheric properties LUTs by MODTRAN.

Atmospheric property	Unit	Values/type ^a
Visibility	km	4–100
Aerosol-type	–	R, M, U

^a We applied the method of Inverse Visibility (IV) to get approximately equal steps in Aerosol Optical Thickness (AOT). In this method, IV values were set equal to 100 divided by the actual visibilities (100 / Visibility). We set the IV values as 1, 2, 3, ..., 25, corresponding to actual visibilities of 100, 50, 33.3, ..., 4 km. Then we calculated the atmospheric parameters of L_o , G, and S by running MODTRAN for the values of the actual visibilities.

average computation time of ten minutes. It should be mentioned that the performance of the MOD2SEA model was already evaluated and validated over ODWs of the Dutch Wadden Sea (Arabi et al., 2016) while the results have shown significant improvements in both the atmospheric correction and MOD2SEA WCC-retrievals in comparison to the standard MERIS Case 2 regional (C2R) processor. Therefore, validation of generated MOD2SEA-WCC maps was considered to fall outside the scope of the present research.

5. Results

5.1. Generating OSW and ODW maps from MERIS/OLCI images by applying the NIBEI

Fig. 5 presents OSW and ODW maps generated by applying the NIBEI on the same MERIS and OLCI images described in Table 6. ODWs are shown in dark-blue, where OSWs are shown in grey. Land regions, including exposed tidal flats (presented by L in the figures' legends), are in black. The sensor and tidal phase at the time of the satellite overpass are indicated above each map.

The number of pixels detected by the NIBEI varies in the different maps. The exact number of these pixels (in percentage) are presented in Table 9. Tides change the water level and water turbidity by releasing water inflows from the North Sea into the Dutch Wadden Sea (Arabi et al., 2016). Spatial variability of WCCs may also change in different

dates, SZAs, and seasons (Arabi et al., 2018). As a result, the extent of OSWs varies in different satellite images captured under different tidal phases and dates (Elevedt et al., 2014). Moreover, there are variations between the exposed “dry” seabed pixels flagged as land (exposed tidal flats) during the low tidal phase (Table 9: ~1%–3% of the images), as the tide varies for the different images captured within the different tidal phase. Table 9 presents the exact number of OSW-pixels and land-pixels for each satellite image separately. The estimates are calculated based on the number of OSW/land pixels divided by the whole scene pixels × 100.

5.2. Improving the reliability of water retrieval algorithms by applying the NIBEI

Fig. 6 presents the generated maps of TOA radiance spectral residual errors (RMSE: [W m⁻² sr⁻¹ μm⁻¹]) computed between the best fits of the observed and simulated MOD2SEA-TOA radiances without (left panel) and with (right panel) implementing the NIBEI.

As the left panel of Fig. 6 shows, the generated maps of error estimates have a high spatial variation (RMSE [W m⁻² sr⁻¹ μm⁻¹]: 0–100%) in different parts of the study area for the MERIS and OLCI images captured during high and low tidal phases when the NIBEI is not applied. The highest error estimates (RMSE ≥ 70%) mainly occur in the central parts of the Dutch Wadden Sea nearby the internal islands as well as the areas close by the shore. As a result, the retrieved WCCs (Chla [mg m⁻³], SPM [g m⁻³], and CDOM absorption at 440 nm [m⁻¹]) from images will remain questionable over these regions. As the right panel of this figure presents, applying the NIBEI has helped to flag these high error estimate regions while the remaining areas have very low error estimates (i.e., ODWs located mainly the external parts of the Dutch Wadden Sea in the neighborhood of the North Sea as well as the IJsselmeer lake: RMSE < 20%). Fig. 7 shows the scatter plots of simulated MOD2SEA-TOA radiances against image-pixel radiances over discriminated OSWs and ODWs:

As Fig. 7 presents, there is a much better agreement between the simulated TOA radiances against the observed ones for ODWs (shown in black-circles) in comparison to OSWs (shown in red-triangles) for both MERIS and OLCI images captured during low and high tidal phases, respectively. The related statistical analysis of this evaluation are presented in Tables 10, 11, 12, and 13:

As these tables show, there is a strong agreement between the modeled TOA radiances and the observed ones for all three selected bands (i.e., 490 nm, 560 nm and 665 nm) over ODWs for both low and high tidal phases using the MERIS and OLCI images, respectively ($R^2 \geq 0.95$, RMSE < 1 [W m⁻² sr⁻¹ μm⁻¹], NRMSE ≤ 2.60%, RRMSE < 3%). However, the accuracy of the model to simulate TOA decreases over OSWs for both low and high tidal phases using the MERIS and OLCI images ($R^2 \leq 0.90$, RMSE [W m⁻² sr⁻¹ μm⁻¹] > 1, NRMSE > 3%, RRMSE ≥ 2.5%). Consequently, the retrieved WCCs (Chla, SPM concentrations, and CDOM absorption) will be questionable

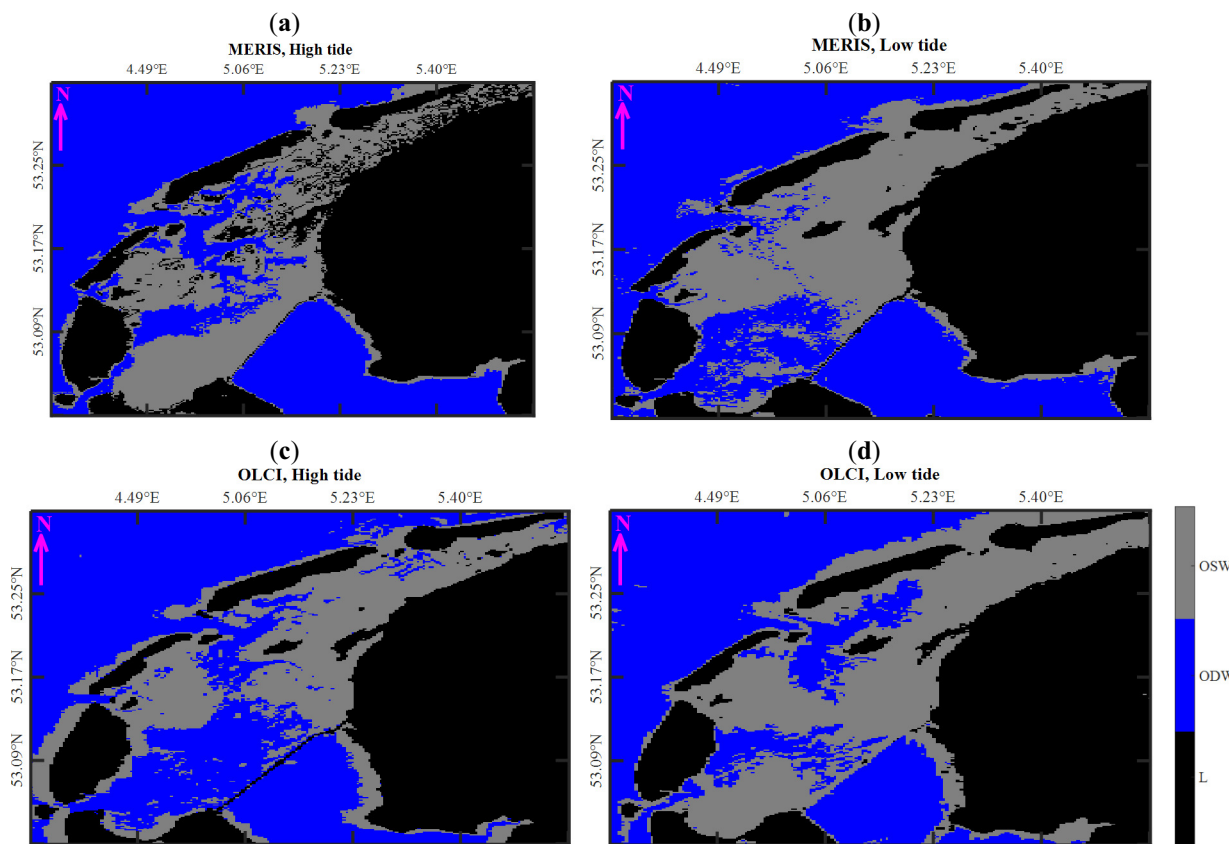


Fig. 5. The generated maps of OSWs and ODWs over the study area from; (a) the MERIS image captured during the high tidal phase; (b) the MERIS image captured during the low tidal phase; (c) the OLCI image captured during the high tidal phase; (d) the OLCI image captured during the low tidal phase.

Table 9

The number of OSW-pixels and land-pixels in percentage for each satellite image.

Satellite sensor	Tidal phase	OSW-pixels (%)	Land-mask pixels (%)
MERIS	High tide	21%	42%
MERIS	Low tide	23%	40%
OLCI	High tide	23%	39%
OLCI	Low tide	29%	38%

over these OSWs due to very high spectral residual errors while the NIBEI is not implemented on the images. Additionally, implementing the NIBEI significantly helps to increase the accuracy of the model's TOA simulations for both ODWs and OSWs, and accordingly, reliability of retrieved WCC maps from the images to be used in further processing as desired.

Since the regions masked by the NIBEI are classified as OSWs, it can be said that the effect of the sea-bottom on the satellite observations is one of the main causes of high error estimates over these areas. Although a heterogeneous atmosphere (e.g., the existence of local haze variation) could be another factor influencing the spatial accuracy of the model's simulations (Arabi et al., 2016; Shen and Verhoef, 2010), further investigations showed that mostly similar combinations of visibility and aerosol type were present over OSWs and ODWs at time of satellite overpass in the study area. The maps of aerosol type (Fig. 8) and visibility (Fig. 9) are generated by using the MOD2SEA model, and readers are referred to Arabi et al. (2016) for more information on the implemented approach to generate these maps.

Comparing the left and right panels of Figs. 8 and 9, it can be observed that the high spectral residual errors of the model's simulations over OSWs, detected by the NIBEI, are independent of variations in

atmospheric type and visibility. For example, the atmospheric type shows similar combinations of maritime and urban over both OSWs and ODWs in Fig. 8(a) and (b). The story is the same for visibility, which is homogenous over discriminated OSWs and ODWs in Fig. 9(a) and (b). As a result, it can be said that the effect of the sea-bottom can be considered as the main reason for the model's failure to simulate MOD2SEA-TOA radiances accurately over OSWs of the study area (Arabi et al., 2018; Yu et al., 2016a, 2016b). Therefore, it can be concluded that applying the NIBEI on MERIS and OLCI images improve the reliability and consistency of generated WCC maps. The OSW pixels that are contaminated with the sea-bottom effect were properly flagged by NIBEI. However, it will remain a challenge to differentiate the combined effects of sea-bottom, water constituents, and atmosphere using TOA spectra alone. This conclusion does not necessarily mean that applying the NIBEI leads to an increase in the accuracy of the WCC retrievals in ODWs. The accuracy of the WCC retrievals by using a water retrieval algorithm is dependent on other factors such as the suitability of the applied water retrieval algorithm, a model's IOPs parametrizations, sensor characteristics, etc., and is independent of the NIBEI performance. For example, an increase in spatial and spectral resolutions leads to having more spectral information and accordingly leads to improved accuracy of WCC-retrievals (Lee and Carder, 2002). However, this task falls outside the scope of the present study.

5.2.1. Generating reliable WCC maps over ODWs from satellite images

Figs. 10–12 present the generated maps of Chla concentration [mg m^{-3}], SPM concentration [g m^{-3}], and CDOM absorption at 440 nm [m^{-1}] using the MOD2SEA model from the MERIS and OLCI images, respectively.

As Fig. 10 shows, the retrieved Chla concentrations [mg m^{-3}] mainly show high estimates (~ 100 [mg m^{-3}]), nearby the coasts, surrounding islands of the Dutch Wadden Sea (Fig. 10(b), (c), (d)),

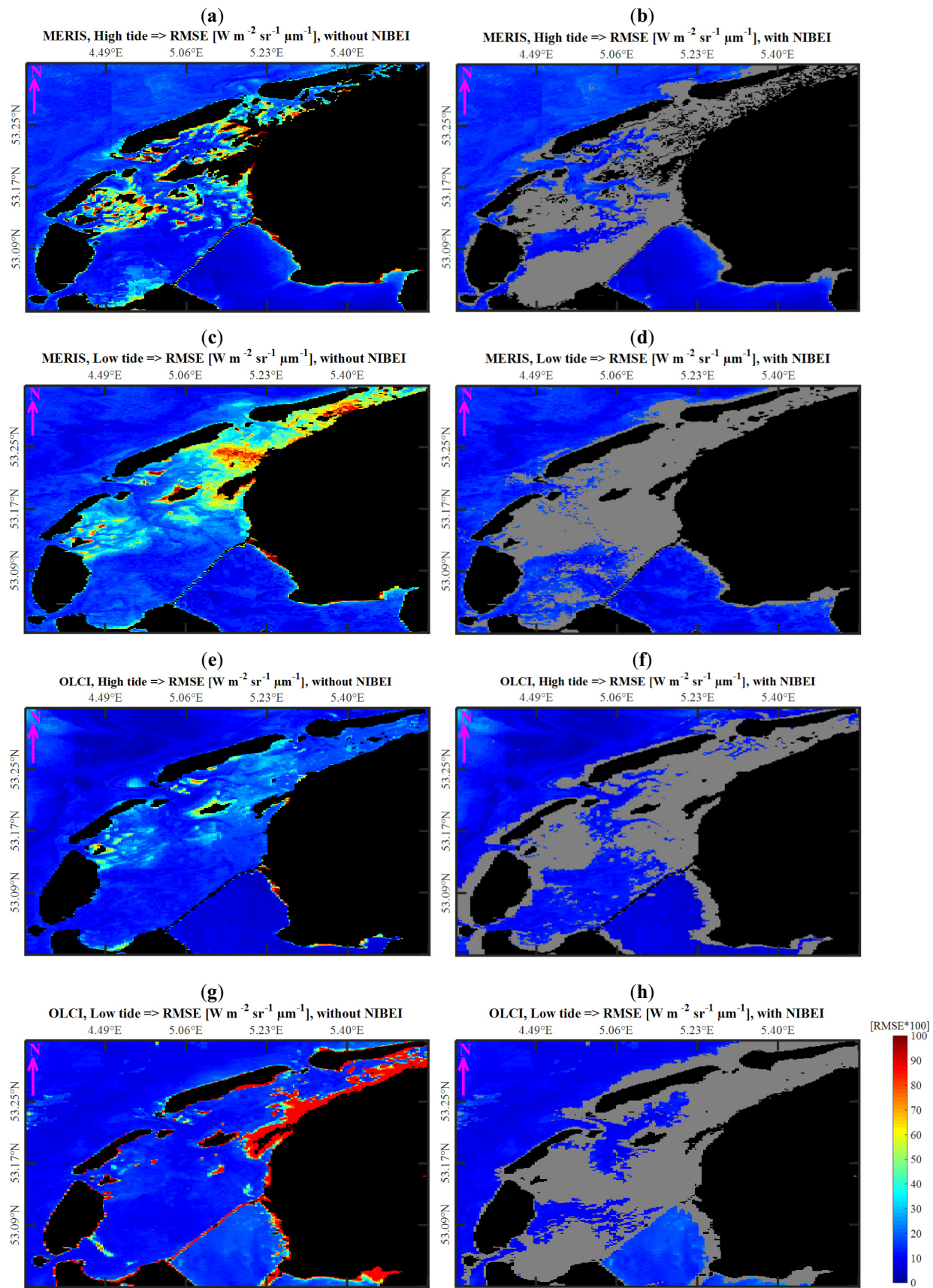


Fig. 6. The generated maps of RMSE(%) [$\text{W m}^{-2} \text{sr}^{-1} \mu\text{m}^{-1}$] estimates between the best fits of observed TOA radiances at satellite image-pixels and simulated TOA radiances by the MOD2SEA model over the study area from; row 1: (a) the MERIS image captured during the high tidal phase (a) without and (b) with applying the NIBEI; row 2: the MERIS image captured during the low tidal phase (c) without and (d) with applying the NIBEI; row 3: the OLCI captured during the high tidal phase (e) without and (f) with applying the NIBEI; row 4: the OLCI image captured during the low tidal phase (g) without and (h) with applying the NIBEI.

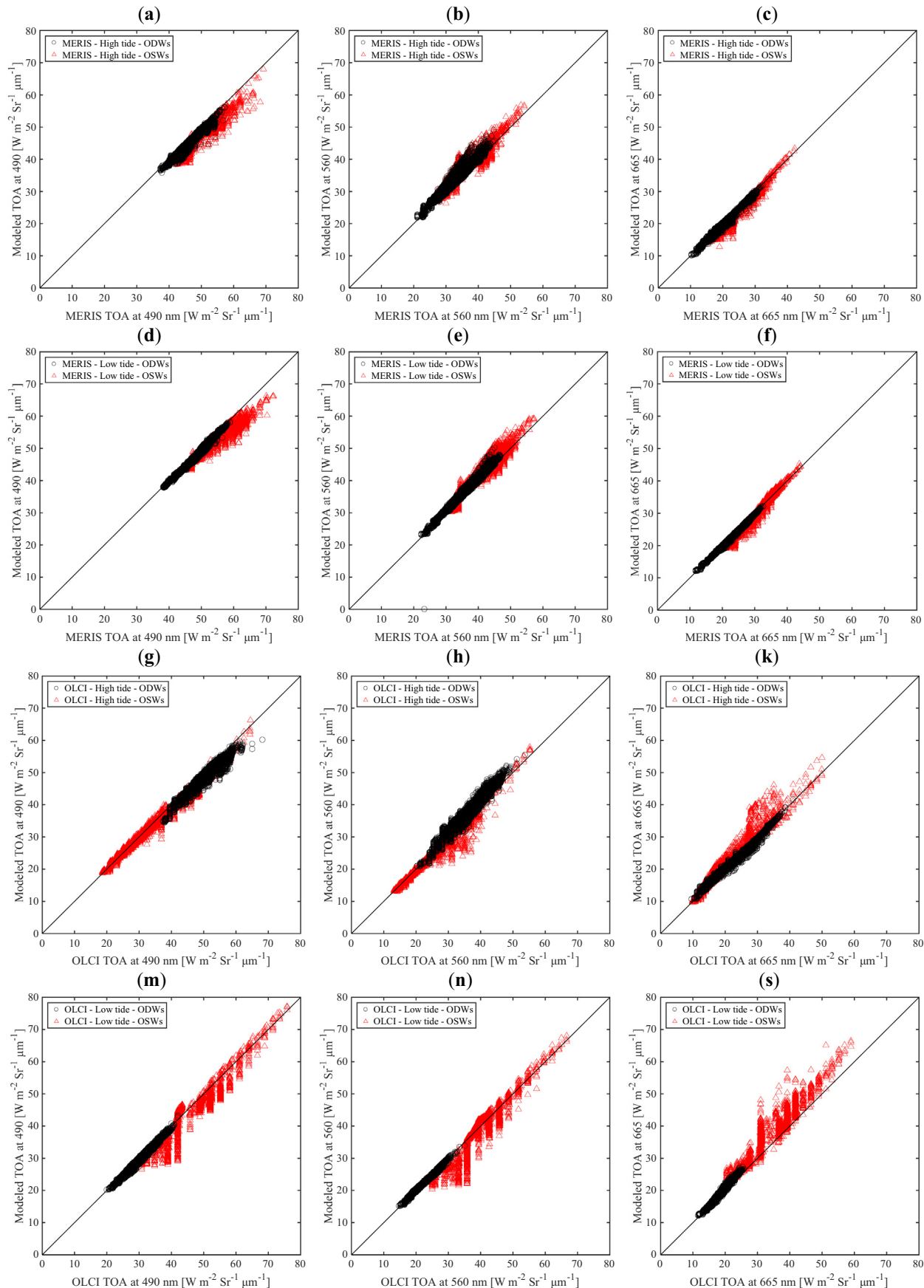


Fig. 7. Comparison between the MOD2SEA model's best-fit spectra and observed TOA radiances [$\text{W m}^{-2} \text{ sr}^{-1} \mu\text{m}^{-1}$] over the study area for the band centers of **column 1:** 490 nm; **column 2:** 560 nm; and **column 3:** 665 nm, and from **row 1:** the MERIS image captured during high tidal phase; **row 2:** the MERIS image captured during low tidal phase; **row 3:** the OLCI captured during high tidal phase; **row 4:** the OLCI image captured during low tidal phase.

Table 10

Evaluation of the MOD2SEA model's best-fit spectra against observed TOA radiances over the study area from the MERIS image captured during the high tidal phase.

Statistical analysis	R ²		RMSE [W m ⁻² sr ⁻¹ μm ⁻¹]		NRMSE (%)		RRMSE (%)	
	ODWs	OSWs	ODWs	OSWs	ODWs	OSWs	ODWs	OSWs
490 nm	0.97	0.85	0.52	1.45	2.60	5.10	1.20	2.86
560 nm	0.98	0.83	0.80	1.60	2.33	5.70	2.65	4.10
665 nm	0.99	0.89	0.41	1.08	1.72	3.36	2.51	3.49

while a maximum values of Chla estimates (≥ 100 [mg m⁻³]) can be observed in the IJsselmeer lake (Fig. 10(a)). These values decrease (~ 60 [mg m⁻³]) while moving from the shores to the internal parts of the Dutch Wadden Sea and reach their lowest amounts (< 20 [mg m⁻³]) in the external parts of the Dutch Wadden Sea in the vicinity of the North Sea for all maps. However, fairly high spatial and temporal variability of Chla concentrations [mg m⁻³] can be observed on various dates. For example, a wider extent of the IJsselmeer lake shows high values of Chla estimates (~ 100 [mg m⁻³]) in Fig. 10(b) and (d) in comparison to Fig. 10(a) and (c).

Fig. 11 presents the generated maps of retrieved SPM concentrations [g m⁻³] over the study area using the same MERIS and OLCI images:

As Fig. 11 shows, the maps of retrieved SPM concentrations [g m⁻³] show the same variation range (0–80 [g m⁻³]) and similar spatial variability for all dates. The SPM concentrations show lower values in the proximity of the North Sea and the IJsselmeer lake (0–20 [g m⁻³]) and higher values nearby the islands.

Fig. 12 presents the generated CDOM absorption at 440 nm [m⁻¹] from the same MERIS and OLCI images.

As it was explained in Section 4.4.2.1, to speed up the process, only five steps of CDOM absorption at 440 nm [m⁻¹] (i.e., [0], [0.5], [1], [1.5] and [2]) were considered into the MOD2SEA WCC-retrievals. Therefore, the spatial variability of CDOM absorption at 440 nm [m⁻¹] is limited to these five values, as are presented in five colours in the legend of the figure.

As Fig. 12 presents, the CDOM absorption at 440 nm [m⁻¹] shows a spatial variability with higher values (≥ 0.5 [m⁻¹]) nearby the coasts and lower values in the North Sea waters (< 0.5 [m⁻¹]). Furthermore, the retrieved CDOM absorption at 440 nm [m⁻¹] has similar spatial variability with retrieved Chla concentrations [m⁻³] (Fig. 10) during different tidal phases for all dates. Overall, with respect to complexity of CDOM analytical-retrieval from satellite images in shallow waters, the generated CDOM absorption at 440 nm [m⁻¹] maps in this research can be regarded as satisfactory enough (Beltrán-Abaunza et al., 2014; Brezonik et al., 2015; Campbell et al., 2011; Kutser et al., 2005a, 2005b; Yu et al., 2016a, 2016b).

6. Discussion

In many coastal areas, the sea-bottom effect contributes to the observed R_{rs} values, both at the water surface and the satellite level (Lee and Carder, 2002). This can interfere with the correct retrieval of WCCs from hyperspectral or multi-spectral satellite sensors depending on local water depth and transparency of the water (Lee et al., 1999; Martinez-carranza and Calway, 2012). Although bathymetry maps can be used to determine the water depth in remote sensing studies of

coastal areas (Pattanaik et al., 2015), these maps are not always available for all regions (Giardino et al., 2012). On the other hand, the sea-bottom effect varies depending on water column attenuation, bottom albedo, substrate type, and water depth variation in tidal areas (Giardino et al., 2014; Maritoren et al., 1994; Mgengel and Spitzer, 1991). Therefore, using bathymetry maps cannot always improve the accuracy of WCC products over shallow tidal areas. However, the WCC products may be able to improve the accuracy of satellite-derived bathymetry maps.

In this paper, we extended the 2SeaColour model by incorporating the sea-bottom effect for modeling of the above water leaving remote sensing reflectance [sr⁻¹] as a function of water constituents' concentrations (i.e., Chla, SPM, CDOM), bottom albedo and water depth. The modified model, called Water - Sea Bottom (WSB), was used to better understand the effect of bottom albedo on field and satellite observations of ocean colour. We found that all parts of R_{rs} spectra are affected by water depth in various ways. However, in the NIR, the R_{rs} spectral shapes are nearly insensitive to WCCs, and spectra only increase in magnitude with water turbidity and bottom albedo (Fig. 3). As the main outcome of this investigation, we defined the novel index, the NIBEI, as the ratio of R_{rs} values/TOA radiances at 750 nm/900 nm to discriminate OSWs contaminated by sea-bottom effects. The NIBEI threshold value for OSWs was NIBEI > 2.67 using R_{rs} values (Section 4.2) and 2.67 ≤ NIBEI ≤ 4.9 using TOA radiances (Section 4.3).

6.1. The NIBEI applications in satellite remote sensing of water quality

In this paper, we tested the application of the NIBEI “for: i) generating shallow vs. optically deep water maps and ii) generating more reliable WCCs maps from satellite images.”

In Section 5.1., we showed that implementing the proposed NIBEI makes it possible to generate OSW/ODW maps from MERIS and OLCI images over the Dutch Wadden Sea (Fig. 5). Generated OSW/ODW maps over highly varied shallow tidal waters are vital for water quality monitoring and management (Eleveld et al., 2014). As shown in Fig. 3, the sea-bottom effect can have an influence on the blue-green part of R_{rs} spectrum for water depths even up to 50 m if the water is clear enough. This interferes with accurate retrieval of WCCs over OSWs if not treated properly. Therefore, it is essential to accurately determine the location of ODWs from satellite images before establishing autonomous in-situ stations or doing fieldwork measurements.

In Section 5.2., we showed that applying the proposed NIBEI improves the accuracy of the MOD2SEA model's performance to simulate TOA radiances by excluding OSWs from the consideration of the model's simulations. It is also worth mentioning that there were regions with low spectral residual errors detected as OSWs masked from the

Table 11

Evaluation of the MOD2SEA model's best-fit spectra against observed TOA radiances over the study area from the MERIS image captured during the low tidal phase.

Statistical analysis	R ²		RMSE [W m ⁻² sr ⁻¹ μm ⁻¹]		NRMSE (%)		RRMSE (%)	
	ODWs	OSWs	ODWs	OSWs	ODWs	OSWs	ODWs	OSWs
490 nm	0.99	0.79	0.38	1.43	1.83	5.38	0.81	2.56
560 nm	0.99	0.84	0.51	1.47	2.08	5.73	1.54	3.39
650 nm	0.99	0.90	0.23	1.06	1.10	3.10	1.20	2.49

Table 12

Evaluation of the MOD2SEA model's best-fit spectra against observed TOA radiances over the study area from the OLCI captured during the high tidal phase.

Statistical analysis	R ²		RMSE [W m ⁻² sr ⁻¹ μm ⁻¹]		NRMSE (%)		RRMSE (%)	
	ODWs	OSWs	ODWs	OSWs	ODWs	OSWs	ODWs	OSWs
490 nm	0.95	0.89	0.86	2.03	1.96	3.08	1.83	3.05
560 nm	0.96	0.88	0.98	2.14	2.45	4.22	2.32	4.73
665 nm	0.98	0.89	0.53	2.38	1.68	5.43	2.99	7.87

images by applying the NIBEI (Fig. 6). Indeed in these areas, the pixel TOA spectra match well with at least one of the generated TOA radiances LUTs by the MOD2SEA model. We know from the NIBEI that the water is optically shallow in these areas. Therefore, for these regions, applying the NIBEI is even more useful since it can flag for OSWs even if estimated residual spectral errors are small. Caution is advised as the retrieved WCCs in these areas are probably incorrect due to the sea-bottom effect.

In Section 5.2.1, we generated reliable WCC maps (i.e., Chla concentration [mg m⁻³], SPM concentration [g m⁻³], and CDOM absorption at 440 nm [m⁻¹]) over distinct ODWs by the NIBEI where there was a strong agreement between simulated MOD2SEA-TOA radiances against the observed ones. Generating consistently reliable water quality products (Figs. 10, 11, and 12) creates an excellent opportunity for the long-term spatio-temporal monitoring of the Wadden Sea with respect to the availability of MERIS (2002–2012) and OLCI (2018–present) images. Such information is vital for the maintenance and conservation of this World Heritage site following the recent report of SDGs (i.e., Goal-14: Conserve and sustainably use the oceans, seas, and marine resources) (Marmot and Bell, 2018), the European Water Framework Directive (WFD) and the European Marine Strategy Framework Directive (MSFD) (Doerffer and Fischer, 1994; Eleveld et al., 2007; Enemark, 2005; Kabat et al., 2012). It is also worth mentioning that generating consistently reliable water quality maps has a significant contribution in monitoring, protection, and maintenance of coral reef habitats in many coastal regions. For example, studies have shown that the coral habitat has declined under the stress of poor water quality in the Florida Keys over the past 30 years (Boyer and Jones, 2002; Gardner et al., 2003). Systematic monitoring using reliable WCC maps is a big step forward in supporting their monitoring program which has been implemented over the large extent of the Florida Keys National Marine Sanctuary (Dustan, 1999; Klein and Orlando, 1994; Murdoch and Aronson, 1999; Ogden et al., 1994).

6.2. Advantages/similarities to other bottom-effect indexes

The newly proposed NIBEI in this study is used to readily distinguish OSWs from ODWs prior to the implementation of water retrieval algorithms on satellite imagery in shallow coastal waters. This concept is similar to the Bottom Effect Index (BEI: the band ratio of R_{rs}[690 nm]/R_{rs}[555 nm]) proposed by Li et al. (2017) to quickly identify waters in the Saginaw Bay within Lake Huron for which the sea-bottom reflectance is significant (Li et al., 2017). Indeed the BEI is a metric index that proposes a threshold to classify OSWs (depth ≤ 1.5 m or BEI ≥ 0.2) from ODWs (depth > 1.5 m or BEI < 0.2). However, implementing the BEI requires some ancillary input data such as water

depths and R_{rs} estimations. In order to apply the BEI on satellite imagery, one needs to apply an appropriate atmospheric correction to calculate R_{rs} values. Applying an atmospheric correction is the most challenging part of satellite remote sensing of coastal waters and can easily interfere with the accuracy of retrieved R_{rs} values from TOA radiances. Additionally, implementing the BEI requires the accurate estimation of water depth in the form of bathymetric charts, which may not be easily nor freely available for many coastal areas.

Mckinna and Werdell (2018) developed an approach to flag OSWs using MODIS imagery of the Great Barrier Reef, Australia. However, implementing their approach also requires ancillary input, namely bathymetric data, water clarity, and seafloor albedo, which are not always available for all regions. Thus, it can be said that the big advantage of the NIBEI in comparison to other existing indexes is its independency from various site-specific ancillary data mentioned earlier. In other words, the NIBEI can be directly applied to the satellite image by only having TOA radiances and selecting the proper band centers of 750 nm and 900 nm from any multispectral sensor to detect OSWs.

Another advantage of the NIBEI is its applicability to multi-spectral satellite imagery, while most water retrieval algorithms developed for shallow water require hyperspectral observations. For example, a Semi-Analytical (SA) model was developed by Lee et al. (1998) for simultaneous retrieval of bottom albedo, water depth, total absorption, and total backscattering coefficients from hyperspectral measurements over shallow coastal waters. However, to implement the SA model on multi-spectral satellite imagery, hyperspectral images are required. This, in turn, needs a much larger data storage and longer data processing. Moreover, if the main objective for coastal and oceanic observations is to estimate WCCs, bottom depth, and bottom type, an ideal sensor does not necessarily need hyperspectral bands (Lee and Carder, 2002). Indeed, it might be more suitable and cost-effective to have an adequate number of bands, spatial resolution, and high signal-to-noise ratios (Lee and Carder, 2002). Besides, implementing the SA model on satellite images requires local inputs of empirical coefficients, in-situ measurements of bottom albedo, and water depths to calibrate/validate the model when applied to a new environment. Note that the requirement of the above-mentioned input data and intensive calibration and validation implies that the SA model is very site-specific. In contrast, the NIBEI can easily be applied to other locations, although the threshold values of the NIBEI to differentiate between OSW and ODW are image-specific.

All in all, with respect to the simplicity, rapid data processing, transferability to other regions and no-ancillary data requirement (other than TOA radiances), the proposed NIBEI in this study is able to overcome all the above-mentioned deficits and can make a significant improvement to increasing the reliability of water quality products for

Table 13

Evaluation of the MOD2SEA model's best-fit spectra against observed TOA radiances over the study area from the OLCI image captured during the low tidal phase.

Statistical analysis	R ²		RMSE [W m ⁻² sr ⁻¹ μm ⁻¹]		NRMSE (%)		RRMSE (%)	
	ODWs	OSWs	ODWs	OSWs	ODWs	OSWs	ODWs	OSWs
490 nm	0.99	0.86	0.35	2.70	1.58	6.00	1.29	5.53
560 nm	0.99	0.87	0.27	2.64	1.32	6.34	1.35	6.51
665 nm	0.99	0.86	0.30	2.39	2.11	6.21	1.86	6.58

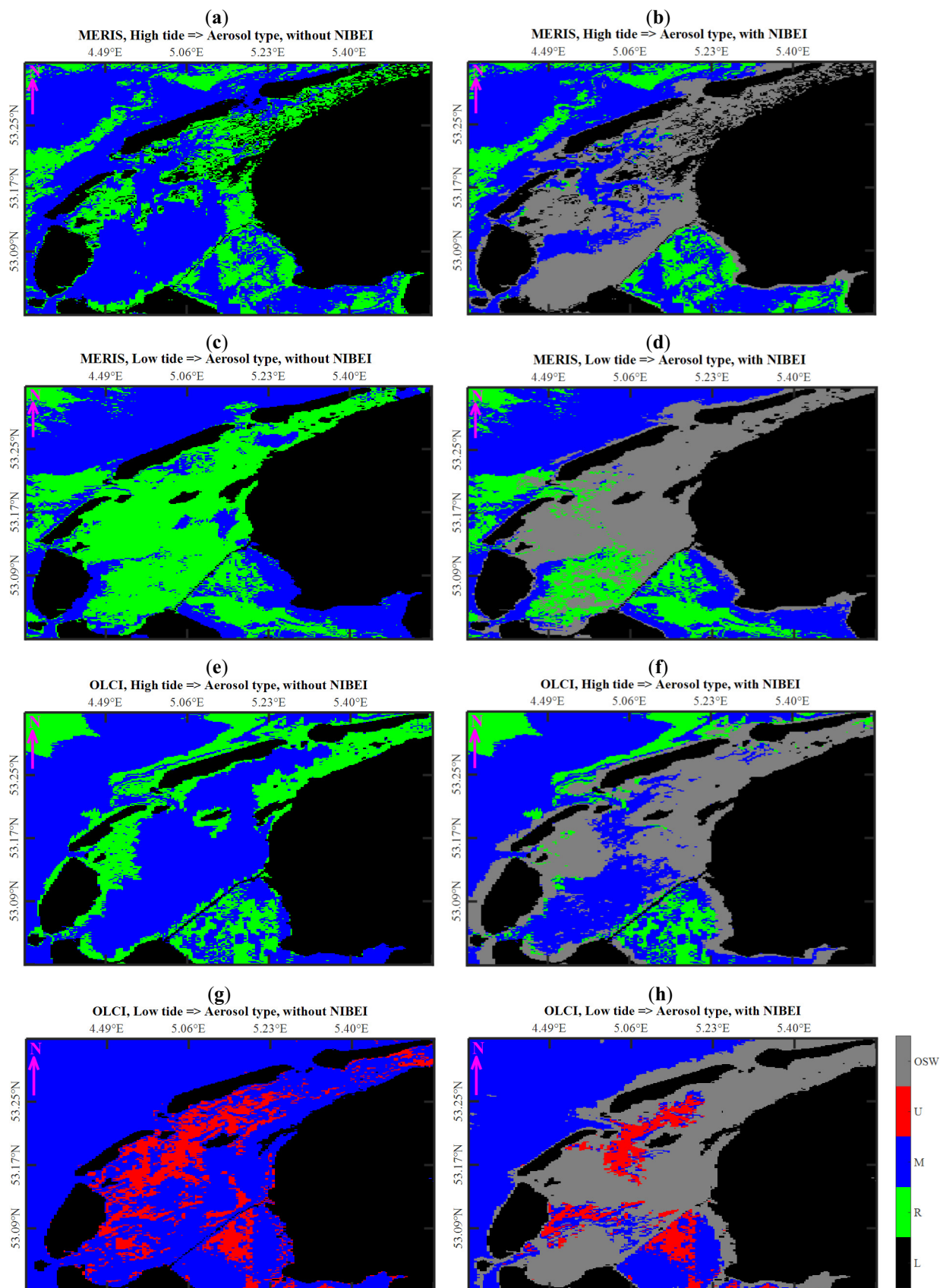


Fig. 8. The generated aerosol type (R: Rural, M: Maritime, U: Urban) maps using the MOD2SEA model over the study area from (a) the MERIS image captured during the high tidal phase; (b) the MERIS image captured during the low tidal phase; (c) the OLCI captured during the high tidal phase; (d) the OLCI image captured during the low tidal phase. The OSWs detected by the NIBEI are shown in grey, and the land regions (L) are shown in black colour, respectively.

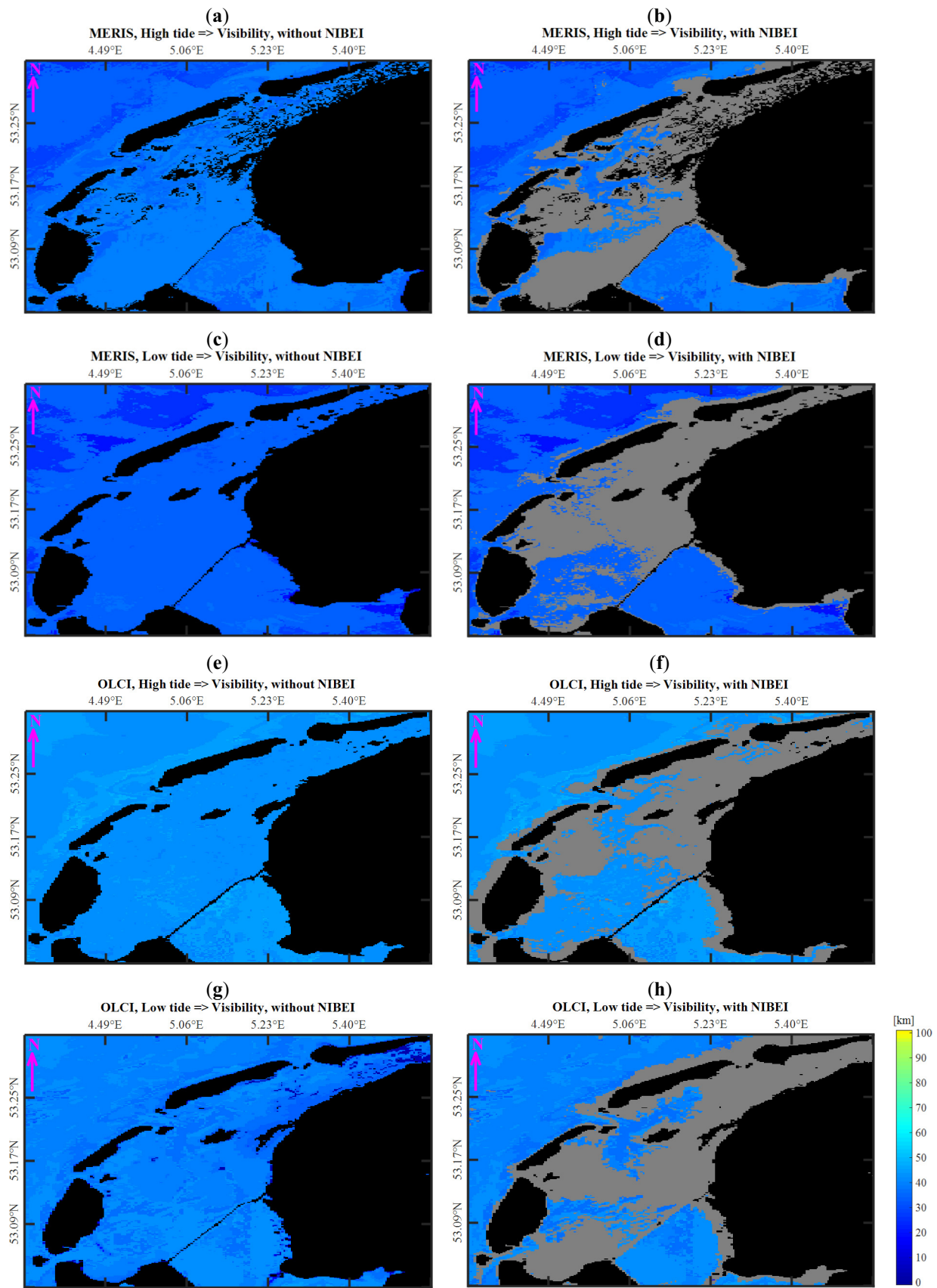


Fig. 9. The generated visibility [km] maps using the MOD2SEA model over study area from (a) the MERIS image captured during the high tidal phase; (b) the MERIS image captured during the low tidal phase; (c) the OLCI captured during the high tidal phase; (d) the OLCI image captured during the low tidal phase.

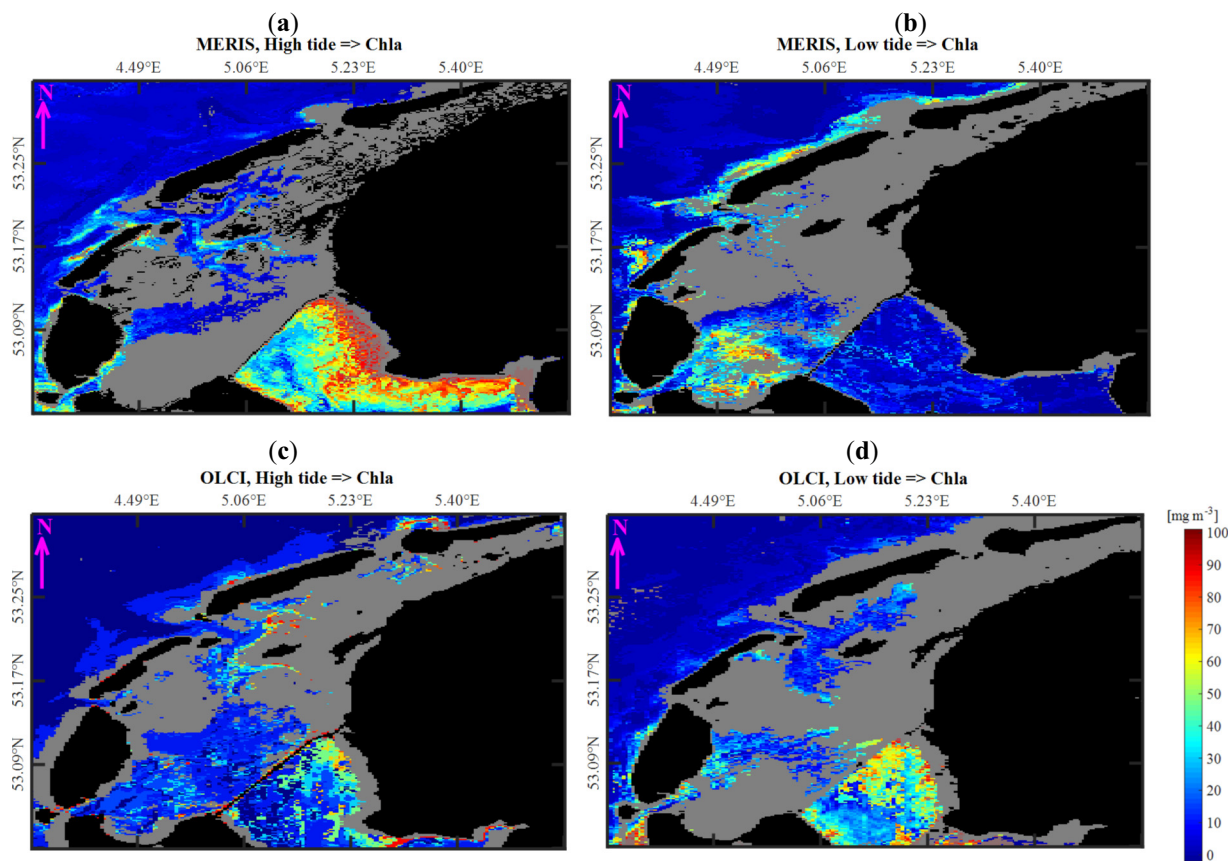


Fig. 10. The generated maps of retrieved Chla concentration [mg m^{-3}] using the MOD2SEA model over the study area from (a) the MERIS image captured during the high tidal phase; (b) the MERIS image captured during the low tidal phase; (c) the OLCI captured during the high tidal phase; (d) the OLCI image captured during the low tidal phase.

challenging shallow coastal regions.

6.3. Recommendation and suggestions

The NIBEI can be easily applied to satellite images captured in different water turbidity, bottom types, observed-illumination geometry, and atmospheric condition to detect OSWs. However, to apply the NIBEI, a proper NIBEI threshold should be determined (Fig. 4). Although determining the appropriate NIBEI threshold per image could be done quickly and easily using visual image-based inspection, these values are not constant for different satellite images and vary slightly considering the date and atmospheric condition of each image (Section 4.3). In the future, it might even be possible to derive the best atmospheric correction from the requirement that NIR spectra for deep waters must have a fixed shape, regardless of WCCs. In that way, it would be possible to apply a fixed value for NIBEI (after atmospheric correction) for all images. However, it will remain a much bigger challenge to differentiate the combination of effects of the sea-bottom, WCCs, and atmospheric properties from radiance spectra alone to retrieve WCCs from OSWs accurately from satellite images (Wang, 2005; Zibordi et al., 2009). Therefore, in this study, we implemented an intermediate approach by flagging OSWs as objects that are too complex for further spectral analysis and to estimate WCCs only from pixels that have been identified as ODWs. This is because, at the TOA level, the NIBEI will be slightly influenced by the atmospheric gain and path radiances. Obviously, after atmospheric correction, one can probably establish fixed thresholds. This is a topic for further investigation.

The proposed NIBEI can be easily applied to Earth Observation data, provided information at band centers 750 nm and 900 nm are available with sufficient spectral resolution, although the required band width

should be considered. Therefore we suggest evaluating the performance of this index to detect OSWs using data from other ocean colour remote sensors like the MODIS, Geostationary Ocean Colour Imager (GOCI), or future Environmental Mapping and Analysis Program (Enmap) products.

As explained in previous sections, the only requirement to apply the NIBEI is TOA radiances recorded at satellite image pixels as the NIBEI is free from local factors such as IOPs parametrizations, empirical coefficients, atmospheric conditions or other ancillary data. The proposed NIBEI is not site-specific and can be easily applied to other locations. We welcome testing the applicability of the proposed NIBEI in other coastal areas to see how broadly applicable this index might be and to what extent our findings could be generalized.

We suggest evaluating the application of the NIBEI in improving the optical remote sensing of bathymetry and benthic habitats in complex non-turbid shallow waters with known high bottom reflectance contributions like the Bahamas and the Florida Keys, USA. Recently there has been a great interest to implement different methods of empirical algorithms, RT modeling, and Artificial Neural Networks to classify bottom types and estimate bathymetry using satellite images in these regions. The results of these studies show that all the tested algorithms perform much better with higher accuracy in OSWs in comparison to ODWs. The reason is that water transparency, bottom reflectance, and atmospheric transmittance combine to give the strongest bottom reflected signal in OSWs (Sandige and Holyer, 1998) while in ODWs, the absorption and scattering of water column and the reflectance of the sea-bottom limit significant bottom reflected radiance (Casey, 2007; Louchard et al., 2003; Mumby et al., 2004; Palandro et al., 2008; Sandige and Holyer, 1998; Stumpf et al., 2006). As a result, all tested algorithms have failed to accurately estimate water depth and bottom

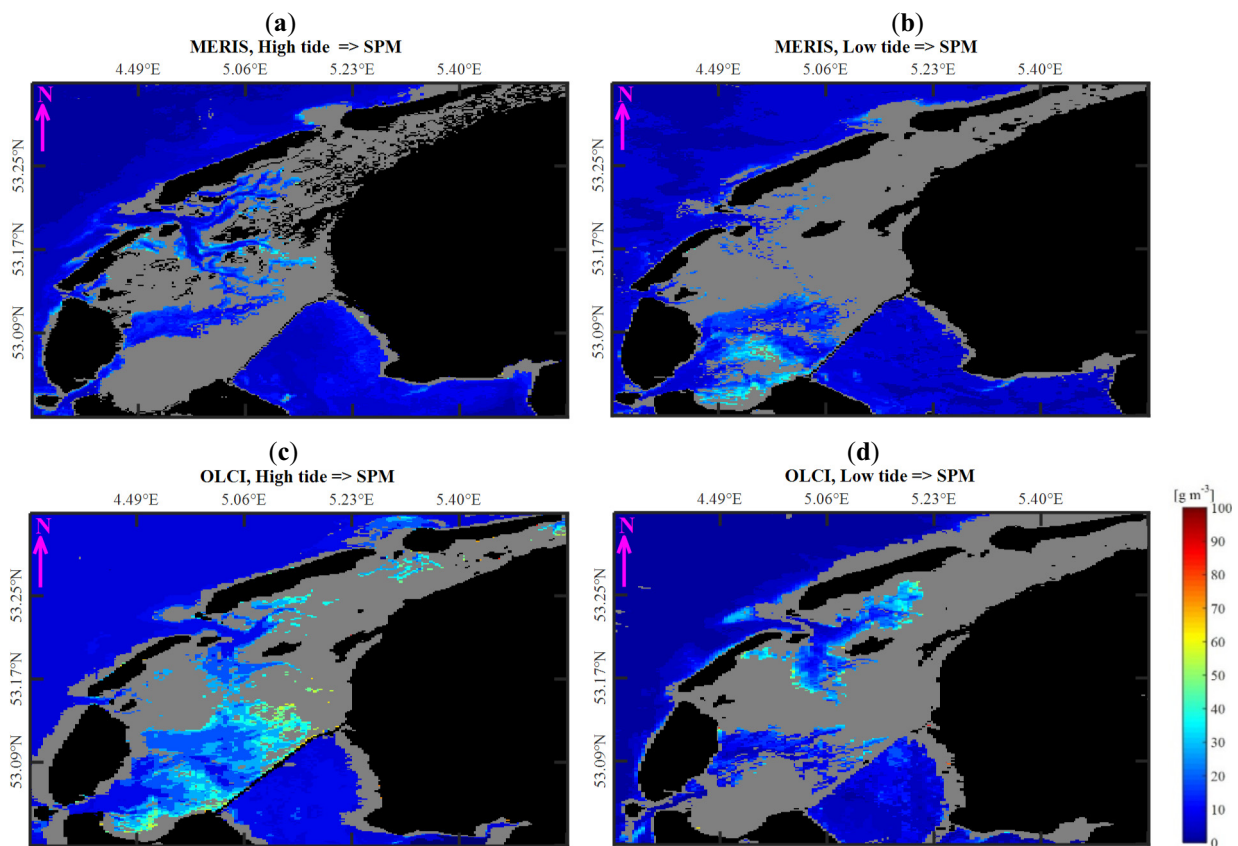


Fig. 11. The generated maps of retrieved SPM concentration [g m^{-3}] using the MOD2SEA model over the study area from (a) the MERIS image captured during the high tidal phase; (b) the MERIS image captured during the low tidal phase; (c) the OLCI captured during the high tidal phase; (d) the OLCI image captured during the low tidal phase.

type in ODWs (Louchard et al., 2003; Palandro et al., 2008; Sandige and Holter, 1998). Therefore, for these studies, the NIBEI can be used in the opposite way to exclude ODWs from water retrievals' consideration before further processing of satellite images. Flagging ODWs in these complex regions not only increases the reliability of the applied models' retrievals by only focusing on OSWs of the study site but also saves time and money by proper determination of OSWs to collect in-situ measurements for the sake of the selected models' calibration and validation.

Eventually, we would like to promote the proposed NIBEI index to be incorporated into image processing software programs (e.g., SeaDAS, ERDAS, SNAP, ENVI) to be used for multi-spectral satellite image processing (e.g., OLCI, Multispectral Instrument (MSI), MERIS, GOCI) over complex shallow areas. This can be feasible by applying an appropriate atmospheric correction method on satellite images and then implementing the NIBEI on estimated R_{rs} images from TOA radiance images to detect OSWs using the fixed threshold of 2.67. This will not only help the rapid detection of OSWs from satellite images but will also benefit the application of other tools such as BOMBER (Bio-Optical Model-Based tool for Estimating water quality and bottom properties from Remote sensing images) (Giardino et al., 2012). BOMBER, promoted on the ENVI, is the only available tool for simultaneous retrieval of water depth, bottom type, and WCCs from satellite images over shallow waters at the moment. BOMBER requires the accurate location of OSWs and ODWs as one of its main input data. By incorporating the NIBEI into image processing software, the resulting discriminated OSW/ODW pixels can then be directly inputted into the BOMBER tool, increasing the accuracy of the final products. These products could later help improve habitat classification, satellite-derived bathymetry, and bottom sediment classification at the low tidal phase.

7. Conclusion

We developed a new model called WSB to incorporate the sea-bottom effect into R_{rs} simulations using RT modeling. From the performed analysis and investigations of this research, we conclude that:

- 1) The addition of the bottom layer to the 2SeaColour model enables simulation of the sea-bottom effect on the observed R_{rs} values and facilitates the development of the NIBEI.
- 2) The NIBEI discriminates OSWs from ODWs on MERIS and OLCI images.
- 3) The exclusion of OSWs from MERIS/OLCI images increases the reliability of the generated WCCs maps over complex shallow waters.

Declaration of competing interests

The authors declare that they have no known competing financial interests or personal relationships that could have appeared to influence the work reported in this paper.

Author's contribution

All authors have made major and unique contributions to this research.

The satellite data from the ESA (European Space Agency) archive of MERIS and OLCI images was download and proceed by Behnaz Arabi. All maps were produced by Behnaz Arabi. Fig. 1 and Fig. 3 were produced by Daphne van der Wal and Wouter Verhoef, respectively. The Matlab code to generate maps and to produce R_{rs} spectra by the WSB model was written by Behnaz Arabi and Wouter Verhoef, respectively.

The WSB model was developed by Wouter Verhoef. Behnaz Arabi

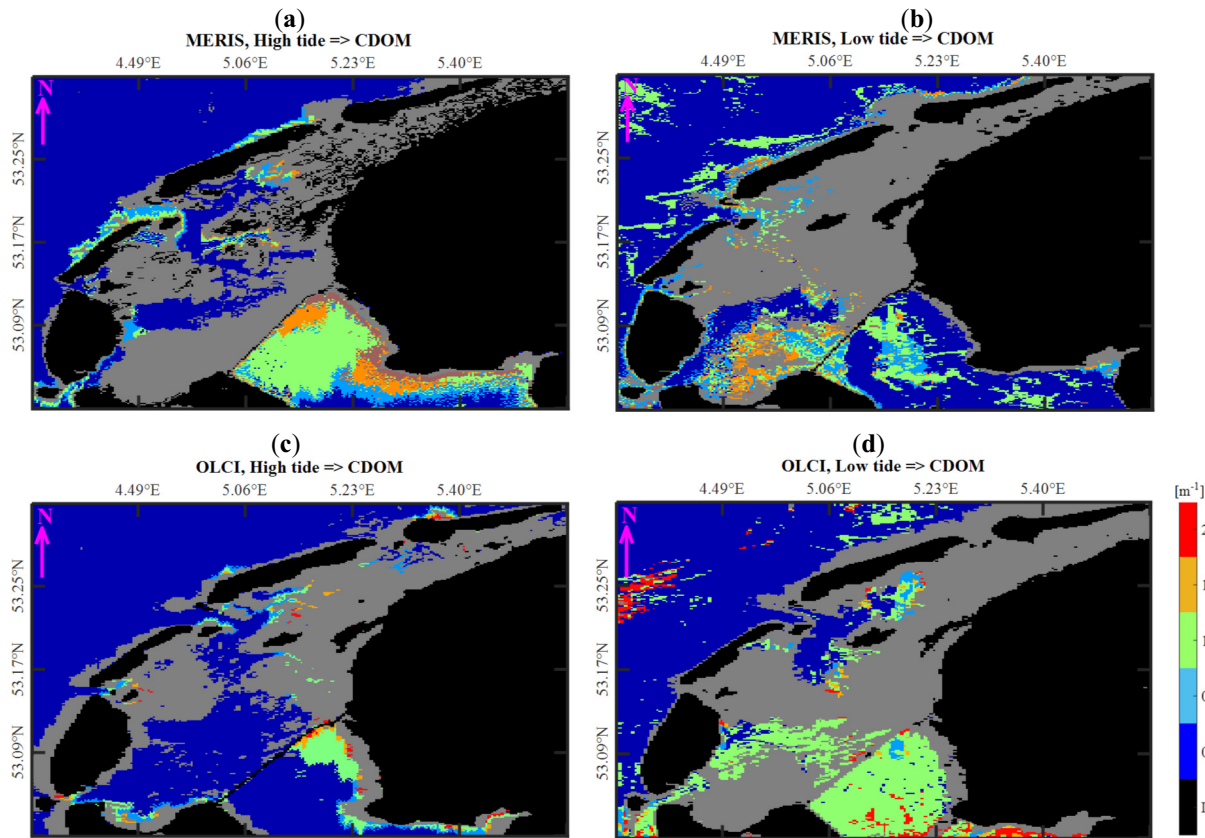


Fig. 12. The generated maps of CDOM absorption at 440 nm [m^{-1}] using the MOD2SEA model over the study area from (a) the MERIS image captured during the high tidal phase; (b) the MERIS image captured during the low tidal phase; (c) the OLCI captured during the high tidal phase; (d) the OLCI image captured during the low tidal phase.

performed MODTRAN and model simulations, data analysis as well as results interpretation. The original manuscript was written by Behnaz Arabi. Appendix A was written by Wouter Verhoef. In addition, Wouter Verhoef, Suhyb Salama and Daphne van der Wal supervised the research and discussed the results and provided a substantial contribution in revising the manuscript at all stages. Jaime Pitacrh revised the manuscript and provided useful suggestions and editions to improve the overall quality of the manuscript.

All authors have read and approved the final version of this manuscript.

Appendix A. Water layer optical properties in the WSB model

In the WSB model, a numerically safe solution of radiative transfer is applied that has been adapted from the 4SAIL vegetation canopy reflectance model (Verhoef et al., 2007). The numerical safety refers to the treatment of the possible singularity occurring when $k = m$, where m is the eigenvalue or the diffusion exponent of the two-stream system. Since the extinction coefficient k depends only on the solar zenith angle, and m depends on the spectral absorption properties of the medium, in many cases, the possibility exists that a combination of solar zenith angle and wavelength occurs under which this singularity can accidentally come to expression in the form of numerical instability.

Radiative transfer in water can be described with a similarity transformation that forces quasi-isotropic scattering, which means that only two scattering coefficients are needed, namely σ and s , the hemispheric (back)scattering coefficients for incident diffuse hemispheric light and direct sunlight, respectively. In this case, the diffusion exponent is found from:

$$m = \sqrt{\kappa(\kappa - 2\omega)} = 2\sqrt{1 - \omega}. \quad (\text{A1})$$

The infinite reflectance is given by

$$r_\infty = \frac{\omega}{\kappa - \omega + m} = \frac{\omega}{2 - \omega + 2\sqrt{1 - \omega}}. \quad (\text{A2})$$

In terms of $x = b_b/a$, one can write

Acknowledgments

We would like to thank the European Space Agency (ESA) for providing the OLCI and MERIS images of this research within the framework of the Integrated Network for Product. This research was supported by The International Institute for Geo-Information Science and Earth Observation (ITC) faculty foundation (ref: IFP17.1.3), University of Twente, the Netherlands.

$$\begin{aligned}
r_\infty &= \frac{\omega}{2 - \omega + 2\sqrt{1 - \omega}} = \frac{\frac{2b_b}{a + 2b_b}}{2 - \frac{2b_b}{a + 2b_b} + 2\sqrt{1 - \frac{2b_b}{a + 2b_b}}} = \frac{2b_b}{2(a + 2b_b) - 2b_b + 2\sqrt{a(a + 2b_b)}} \\
&= \frac{b_b/a}{1 + b_b/a + \sqrt{(1 + 2b_b/a)}} = \frac{x}{1 + x + \sqrt{(1 + 2x)}} \tag{A3}
\end{aligned}$$

From this we also find

$$\begin{aligned}
1 + r_\infty &= \frac{1 + 2x + \sqrt{(1 + 2x)}}{1 + x + \sqrt{(1 + 2x)}} ; \quad 1 - r_\infty = \frac{1 + \sqrt{(1 + 2x)}}{1 + x + \sqrt{(1 + 2x)}} ; \\
\frac{1 + r_\infty}{1 - r_\infty} &= \sqrt{(1 + 2x)} \Rightarrow r_\infty = \frac{\sqrt{(1 + 2x)} - 1}{\sqrt{(1 + 2x)} + 1} \tag{A4}
\end{aligned}$$

To distinguish both infinite reflectances, we write $r_{dd}^\infty = r_\infty$. For the infinite DHRF we find

$$\begin{aligned}
r_{sd}^\infty &= \frac{s(1 + r_\infty)}{k + m} = \frac{\frac{b_b}{\mu_w(a + 2b_b)} \frac{2\sqrt{1 + 2x}}{\sqrt{1 + 2x} + 1}}{\frac{1}{\mu_w} + m} = \frac{\frac{x}{\mu_w(1 + 2x)} \frac{2\sqrt{1 + 2x}}{\sqrt{1 + 2x} + 1}}{\frac{1}{\mu_w} + \frac{2}{\sqrt{1 + 2x}}} = \frac{\frac{2x}{\sqrt{1 + 2x} + 1}}{\sqrt{1 + 2x} + 2\mu_w} \\
&= \frac{\frac{2x}{\sqrt{1 + 2x} + 1} \frac{\sqrt{1 + 2x} - 1}{\sqrt{1 + 2x} - 1}}{\sqrt{1 + 2x} + 2\mu_w} = \frac{\sqrt{1 + 2x} - 1}{\sqrt{1 + 2x} + 2\mu_w} \tag{A5}
\end{aligned}$$

The other important quantities of the model are given without derivation:

$$J_1 = \begin{cases} \frac{e^{-mcd} - e^{-kcd}}{k - m} & (|k - m| >= 10^{-3}) \\ \frac{1}{2} cd(e^{-mcd} + e^{-kcd}) \left[1 - \frac{1}{12} (k - m)^2 (cd)^2 \right] & (|k - m| < 10^{-3}) \end{cases} \tag{A6}$$

$$J_2 = \frac{1 - e^{-(k+m)cd}}{k + m} \tag{A7}$$

$$\rho_{dd} = r_\infty \frac{1 - e^{-2mcd}}{1 - r_\infty^2 e^{-2mcd}} ; \quad \tau_{dd} = \frac{1 - r_\infty^2}{1 - r_\infty^2 e^{-2mcd}} e^{-mcd} \tag{A8}$$

$$\rho_{sd} = s(1 + r_\infty) \frac{J_2 - r_\infty e^{-mcd} J_1}{1 - r_\infty^2 e^{-2mcd}} ; \quad \tau_{sd} = s(1 + r_\infty) \frac{J_1 - r_\infty e^{-mcd} J_2}{1 - r_\infty^2 e^{-2mcd}} \tag{A9}$$

The function J_1 was designed to intercept the (near) singularity occurring when k approaches m . From Eq. (A6) one can see that not only the case of the exact singularity is handled, but also a narrow region around it, where $|k - m| < 10^{-3}$. This guarantees a completely smooth behavior of this function, without any sign of numerical instability.

References

- Ackleson, S.G., 2003. Light in shallow waters: a brief research review. Limnol. Oceanogr. 48 (Part 2), 323–328. https://doi.org/10.4319/lo.2003.48.1_part_2.00323.
- Albert, A., Gege, P., 2006. Inversion of irradiance and remote sensing reflectance in shallow water between 400 and 800 nm for calculations of water and bottom properties. Appl. Opt. 45 (10), 2331–2343. <https://doi.org/10.1364/AO.45.002331>.
- Albert, A., Mobley, C., 2003. An analytical model for subsurface irradiance and remote sensing reflectance in deep and shallow case-2 waters. Opt. Express 11 (22), 2873–2890. <https://doi.org/10.1364/OE.11.002873>.
- Ambarwulan, W., Salama, M.S., Mannaerts, C.M., Verhoeft, W., 2011. Estimating specific inherent optical properties of tropical coastal waters using bio-optical model inversion and in situ measurements: case of the Berau estuary, East Kalimantan, Indonesia. Hydrobiologia 211<https://doi.org/10.1007/s10750-010-0473-7>. 658–197.
- Ambarwulan, W., Verhoeft, W., Mannaerts, C.M., Salama, M.S., 2012. Estimating total suspended matter concentration in tropical coastal waters of the Berau estuary, Indonesia. Int. J. Remote Sens. 33 (2012), 4919–4936. <https://doi.org/10.1080/01431161.2011.583289>.
- Ammenberg, P., Flink, P., Lindell, T., Pierson, D., Strömbeck, N., 2002. Bio-optical modelling combined with remote sensing to assess water quality. Int. J. Remote Sens. 23 (2002), 1621–1638. <https://doi.org/10.1080/01431160110071860>.
- Arabi, B., Salama, M.S., Wernand, M.R., Verhoeft, W., 2016. MOD2SEA: a coupled atmosphere-hydro-optical model for the retrieval of chlorophyll-a from remote sensing observations in complex turbid waters. Remote Sensing. Special Issue: Water Optics and Water Colour Remote Sensing 8, 722. <https://doi.org/10.3390/rs8090722>.
- Arabi, B., Salama, M.S., Wernand, M.R., Verhoeft, W., 2018. Remote sensing of water constituent concentrations using time series of in-situ hyperspectral measurements in the Wadden Sea. Remote Sens. Environ. 216, 154–170. <https://doi.org/10.1016/j.rse.2018.06.040>.
- Barbier, E., 2011. The policy challenges for green economy and sustainable economic development. Nat. Res. Forum 35, 233–245. <https://doi.org/10.1111/j.1477-8947.2011.01397.x>.
- Beltrán-Abaunza, J.M., Kratzer, S., Brockmann, C., 2014. Evaluation of MERIS products from Baltic Sea coastal waters rich in CDOM. Ocean Sci. 10 (2014), 377–396. <https://doi.org/10.5194/os-10-377-2014>.
- Berk, A., Anderson, G.P., Acharya, P.K., Shettle, E.P., 2011. MODTRAN 5.2.1 User's Manual.
- Beukema, J.J., 1976. Biomass and species richness of the macro-benthic animals living on the tidal flats of the Dutch Wadden Sea. Neth. J. Sea Res. 10 (2), 236–261. [https://doi.org/10.1016/0077-7579\(76\)90017-X](https://doi.org/10.1016/0077-7579(76)90017-X).
- Boere, G.C., Piersma, T., 2012. Flyway protection and the predicament of our migrant birds: a critical look at international conservation policies and the Dutch Wadden Sea. Ocean & Coastal Management 68, 157–168. <https://doi.org/10.1016/j.ocecoaman.2012.05.019>.
- Boyer, J.N., Jones, R.D., 2002. A view from the bridge: External and internal forces affecting the ambient water quality of the Florida Keys National Marine Sanctuary (FKNMS). In: The Everglades, Florida bay, and Coral Reefs of the Florida Keys: An Ecosystem Sourcebook. CRC Press, Boca Raton, FL, pp. 609–628.
- Brando, V.E., Dekker, A.G., 2003. Satellite hyperspectral remote sensing for estimating estuarine and coastal water quality. IEEE Trans. Geosci. Remote Sens. 41, 1378–1387. <https://doi.org/10.1109/TGRS.2003.812907>.
- Brezonik, P.L., Olmanson, L.G., Finlay, J.C., Bauer, M.E., 2015. Factors affecting the measurement of CDOM by remote sensing of optically complex inland waters. Remote Sens. Environ. 157, 199–215. <https://doi.org/10.1016/j.rse.2014.04.033>.
- Cadée, G.C., 1986. Increased phytoplankton primary production in the Marsdiep area (Western Dutch Wadden Sea). Neth. J. Sea Res. 20, 285–290. [https://doi.org/10.1016/0077-7579\(86\)90050-5](https://doi.org/10.1016/0077-7579(86)90050-5).
- Cadée, G., Hegeman, J., 2002. Phytoplankton in the Marsdiep at the end of the 20th century; 30 years monitoring biomass, primary production, and Phaeocystis blooms. J. Sea Res. 48, 97–110. [https://doi.org/10.1016/S1385-1101\(02\)00161-2](https://doi.org/10.1016/S1385-1101(02)00161-2).
- Campbell, G., Phinn, S.R., Dekker, A.G., Brando, V.E., 2011. Remote sensing of water quality in an Australian tropical freshwater impoundment using matrix inversion and MERIS images. Remote Sens. Environ. 115, 2402–2414. <https://doi.org/10.1016/j.rse.2011.05.003>.
- Cannizzaro, J.P., Carder, K.L., 2006. Estimating chlorophyll-a concentrations from

- remote-sensing reflectance in optically shallow waters. *Remote Sens. Environ.* 101, 3–24. <https://doi.org/10.1016/j.rse.2005.12.002>.
- Carpintero, M., Polo, M.J., Salama, M.S., 2015. Simultaneous atmospheric correction and quantification of suspended particulate matter in the Guadalquivir estuary from Landsat images. *Proceedings of the International Association of Hydrological Sciences* 368, 15–20. <https://doi.org/10.5194/piahs-368-15-2015>.
- Casey, B., 2007. Water and bottom properties of a coastal environment derived from Hyperion data measured from the EO-1 spacecraft platform. *J. Appl. Remote. Sens.* 1, 011502. <https://doi.org/10.1117/1.2822610>.
- Chongya, J., Hongliang, F., 2012. Modeling Soil Reflectance Using a Global Spectral Library San, AGU Fall Meeting. San Francisco. pp. 100101.
- Chybicki, A., 2017. Mapping South Baltic near-shore bathymetry using Sentinel-2 observations. *Polish Maritime Research* 24, 15–25. <https://doi.org/10.1515/pomr-2017-0086>.
- Conger, C.L., Hochberg, E.J., Fletcher, C.H., Atkinson, M.J., 2006. Decorrelating remote sensing color bands from bathymetry in optically shallow waters. *IEEE Trans. Geosci. Remote Sens.* 44, 1655–1660. <https://doi.org/10.1109/TGRS.2006.870405>.
- Dekker, A.G., 1993. Detection of Optical Water Quality Parameters for Eutrophic Waters by High Resolution Remote Sensing. PhD Thesis. English Language. Vrije Universiteit Amsterdam. ISBNs: 9090062343.
- Dierssen, H.M., Zimmerman, R.C., Leathers, R.A., Downes, T.V., Davis, C.O., 2003. Ocean color remote sensing of seagrass and bathymetry in the Bahamas Banks by high-resolution airborne imagery. *Limnol. Oceanogr.* 48 (Part 2), 444–455. https://doi.org/10.4319/lo.2003.48.1.part_2.0444.
- Doerffer, R., Fischer, J., 1994. Concentrations of chlorophyll, suspended matter, and gelbstoff in case II waters derived from satellite coastal zone color scanner data with inverse modeling methods. *Journal of Geophysical Research: Oceans* 99 (C4), 7457–7466. <https://doi.org/10.1029/93JC02523>.
- Doerffer, R., Sorensen, K., Aiken, J., 1999. MERIS potential for coastal zone applications. *Int. J. Remote Sens.* 20, 1809–1818. <https://doi.org/10.1080/014311699212498>.
- Duntley, S.Q., 1942. The optical properties of diffusing materials. *J. Opt. Soc. Am.* 32, 61–70. <https://doi.org/10.1364/JOSA.32.000061>.
- Durand, D., 2000. Optical remote sensing of shallow-water environmental parameters: a feasibility study. *Remote Sens. Environ.* 73, 152–161. [https://doi.org/10.1016/S0034-4257\(00\)00090-0](https://doi.org/10.1016/S0034-4257(00)00090-0).
- Dustan, P., 1999. Coral reefs under stress: sources of mortality in the Florida keys. *Res Forum* 23, 147–155.
- Elefeldt, M.A., van der Woerd, H.J., Beck, H., 2007. Improving the Estimation of North Sea Primary Production: Meris CHL and KD in VGPM. *Envisat Symposium*, Montreux, Switzerland (ESA SP-636).
- Elefeldt, M.A., van der Wal, D., van Kessel, T., 2014. Estuarine suspended particulate matter concentrations from sun-synchronous satellite remote sensing: tidal and meteorological effects and biases. *Remote Sens. Environ.* 143, 204–215 (2014). doi:<https://doi.org/10.1016/j.rse.2013.12.019>.
- Enemark, J., 2005. The Wadden Sea protection and management scheme – towards an integrated coastal management approach? *Ocean & Coastal Management* 48, 996–1015. <https://doi.org/10.1016/j.ocecoaman.2005.03.009>.
- Eugenio, F., Marcello, J., Martin, J., 2015. High-resolution maps of bathymetry and benthic habitats in shallow-water environments using multispectral remote sensing imagery. *IEEE Trans. Geosci. Remote Sens.* 53, 3539–3549. <https://doi.org/10.1109/TGRS.2014.2377300>.
- Gao, J., 2009. Bathymetric mapping by means of remote sensing: methods, accuracy and limitations. *Prog. Phys. Geogr.* 33, 103–116. <https://doi.org/10.1177/030913309105657>.
- Garaba, S.P., Badewien, T.H., Braun, A., Schulz, A.C., Zielinski, O., 2014. Using ocean colour remote sensing products to estimate turbidity at the Wadden sea time series station Spiekeroog. *Journal of the European Optical Society-Rapid publications* 9. <https://doi.org/10.2971/jeos.2014.14020>.
- Garcia, R.A., Lee, Z., Hochberg, E.J., 2018. Hyperspectral shallow-water remote sensing with an enhanced benthic classifier. *Remote Sens.* 10, 147. <https://doi.org/10.3390/rs10010147>.
- Gardner, T.A., Côté, I.M., Gill, J.A., Grant, A., Watkinson, A.R., 2003. Long-term region-wide declines in Caribbean corals. *Science* 301, 958–960. <https://doi.org/10.1126/science.1086050>.
- Giardino, C., Candiani, G., Bresciani, M., Lee, Z., Gagliano, S., Pepe, M., 2012. BOMBER: a tool for estimating water quality and bottom properties from remote sensing images. *Comput. Geosci.* 45, 313–318. <https://doi.org/10.1016/j.cageo.2011.11.022>.
- Giardino, C., Bresciani, M., Cazzaniga, I., Schenk, K., Rieger, P., Braga, F., Matta, E., Brando, V.E., Brando, V.E., 2014. Evaluation of multi-resolution satellite sensors for assessing water quality and bottom depth of Lake Garda. *Sensors* 14, 24116–24131. <https://doi.org/10.3390/s141224116>.
- Giesen, W.B., Katwijk, M.M.V., Hartog, C.D., 1990. Eelgrass condition and turbidity in the Dutch Aquat. Bot. 37, 71–85. [https://doi.org/10.1016/0304-3770\(90\)90065-S](https://doi.org/10.1016/0304-3770(90)90065-S).
- Gitelson, A.A., Schalles, J.F., Hladik, C.M., 2008. Remote chlorophyll-a retrieval in turbid, productive estuaries: Chesapeake Bay case study. *Remote Sens. Environ.* 109, 464–472. <https://doi.org/10.1016/j.rse.2007.01.016>.
- Gons, H.J., Rijkeboer, M., Ruddick, K.G., 2002. A chlorophyll-retrieval algorithm for satellite imagery (Medium Resolution Imaging Spectrometer) of inland and coastal waters. *J. Plankton Res.* 24, 947–951. <https://doi.org/10.1093/plankt/24.9.947>.
- Gordon, H.R., Wang, M., 1994. Retrieval of water-leaving radiance and aerosol optical thickness over the oceans with SeaWiFS: a preliminary algorithm. *Appl. Opt.* 33, 443–452. <https://doi.org/10.1364/AO.33.000443>.
- Green, E.P., Mumby, P.J., Edwards, A.J., Clark, C.D., 1996. A review of remote sensing for the assessment and management of tropical coastal resources. *Coast. Manag.* 24, 1–40. <https://doi.org/10.1080/08920759609362279>.
- Han, B., Loisel, H., Vantrepotte, V., Mériaux, X., Bryère, P., Ouillon, S., Dessailly, D., Xing, Q., Zhu, J., 2016. Development of a semi-analytical algorithm for the retrieval of suspended particulate matter from remote sensing over clear to very turbid waters. *Remote Sens.* 8, 211. <https://doi.org/10.3390/rs8030211>.
- Harvey, E.T., Kratzer, S., Philipson, P., 2014. Satellite-based water quality monitoring for improved spatial and temporal retrieval of chlorophyll-a in coastal waters. *Remote Sens. Environ.* 158, 417–430. <https://doi.org/10.1016/j.rse.2014.11.017>.
- Hieronymi, M., Müller, D., Doerffer, R., 2017. The OC1 neural network swarm (ONNS): a bio-geo-optical algorithm for open ocean and coastal waters. *Front. Mar. Sci.* 4, 140. <https://doi.org/10.3389/fmars.2017.00140>.
- Hommersom, A., 2010. Dense Water and Fluid Sand: Optical Properties and Methods for Remote Sensing of the Extremely Turbid Wadden Sea. PhD Thesis. The Institute for Environmental Studies (IVM). Vrije Universiteit Amsterdam. <http://hdl.handle.net/1871/15939>.
- Hommersom, A., Peters, S.W.M., van der Woerd, H.J., Elefeldt, M.A., Wernand, M.R., de Boer, J., 2010a. Tracing Wadden Sea water masses with an inverse bio-optical and endmember model. *EARSel eProceedings* 9 (1), 1–12.
- Hommersom, A., Wernand, M.R., Peters, S., de Boer, J., 2010b. A review on substances and processes relevant for optical remote sensing of extremely turbid marine areas, with a focus on the Wadden Sea. *Helgol. Mar. Res.* 64, 75–92. <https://doi.org/10.1007/s10152-010-0191-6>.
- Hu, C., 2009. A novel ocean color index to detect floating algae in the global oceans. *Remote Sens. Environ.* 113, 2118–2129. <https://doi.org/10.1016/j.rse.2009.05.012>.
- Hu, C., Carder, K.L., Muller-Karger, F.E., 2000. Atmospheric correction of SeaWiFS imagery over turbid coastal waters: a practical method. *Remote Sens. Environ.* 74, 195–206. [https://doi.org/10.1016/S0034-4257\(00\)00080-8](https://doi.org/10.1016/S0034-4257(00)00080-8).
- Hu, C., Lee, Z., Ma, R., Yu, K., Li, D., Shang, S., 2010. Moderate resolution imaging spectroradiometer (MODIS) observations of cyanobacteria blooms in Taihu Lake, China. *Journal of Geophysical Research: Oceans* 115 (C4). <https://doi.org/10.1029/2009JC005511>.
- IOCCG, 2000. In: Sathyendranath, S. (Ed.), *Remote Sensing of Ocean Colour in Coastal, and Other Optically-Complex, Waters*. Reports of the International Ocean-Colour Coordinating Group, No. 3 IOCCG, Dartmouth, Canada.
- IOCCG, 2012. In: McClain, C.R., Meister, G. (Eds.), *Mission Requirements for Future Ocean-Colour Sensors*. Reports of the International Ocean-Colour Coordinating Group, No. 13 International Ocean-Colour Coordinating Group (IOCCG), Dartmouth, NS, Canada. <https://doi.org/10.25607/OBP-104>. 106pp.
- Kabat, P., Bazelmans, J., van Dijk, J., Herman, P.M.J., van Oijen, T., Pejrup, M., Reise, K., Speelman, H., Wolff, W.J., 2012. The Wadden Sea region: towards a science for sustainable development. *Ocean & Coastal Management* 68, 4–17. <https://doi.org/10.1016/j.ocecoaman.2012.05.022>.
- Klein, C.J., Orlando, S.P., 1994. A spatial framework of water-quality management in the Florida Keys National Marine Sanctuary. *Bull. Mar. Sci.* 54, 1036–1044.
- Kromkamp, J.C., Morris, E.P., Forster, R.M., Honeywill, C., Hagerthey, S., Paterson, D.M., 2006. Relationship of intertidal surface sediment chlorophyll concentration to hyperspectral reflectance and chlorophyll fluorescence. *Estuar. Coasts* 29, 183–196. <https://doi.org/10.1007/BF02781988>.
- Kummu, M., de Moel, H., Ward, P.J., Varis, O., 2011. How close do we live to water? A global analysis of population distance to freshwater bodies. *PLoS One* 6, e20578. <https://doi.org/10.1371/journal.pone.0020578>.
- Kutser, T., 1997. *Estimation of Water Quality in Turbid Inland and Coastal Waters by Passive Optical Remote Sensing*. Dissertations Geophysicales Universitatis Tartuensis. 8. Tartu University Press 1997, pp. 161.
- Kutser, T., Arst, H., Mäekivi, S., Kallaste, K., 1998. Estimation of the water quality of the Baltic Sea and lakes in Estonia and Finland by passive optical remote sensing measurements on board vessel. *Lakes Reserv. Res. Manag.* 3, 53–66. <https://doi.org/10.1111/j.1440-1770.1998.tb00032.x>.
- Kutser, T., Pierson, D.C., Kallio, K.Y., Reinart, A., Sobek, S., 2005a. Mapping lake CDOM by satellite remote sensing. *Remote Sens. Environ.* 94, 535–540. <https://doi.org/10.1016/j.rse.2004.11.009>.
- Kutser, T., Pierson, D.C., Tranvik, L., Reinart, A., Sobek, S., Kallio, K., 2005b. Using satellite remote sensing to estimate the colored dissolved organic matter absorption coefficient in lakes. *Ecosystems* 8, 709–720. <https://doi.org/10.1007/s10021-003-0148-6>.
- Kutser, T., Metsamaa, L., Strömbeck, N., Vahtmäe, E., 2006. Monitoring cyanobacterial blooms by satellite remote sensing. *Estuar. Coast. Shelf Sci.* 67, 303–312. <https://doi.org/10.1016/j.ecss.2005.11.024>.
- Lawford, R., Strauch, A., Toll, D., Fekete, B., Cripe, D., 2013. Earth observations for global water security. *Curr. Opin. Environ. Sustain.* 5, 633–643. <https://doi.org/10.1016/j.cosust.2013.11.009>.
- Lee, Z., Carder, K.L., 2002. Effect of spectral band numbers on the retrieval of water column and bottom properties from ocean color data. *Appl. Opt.* 41, 2191–2201. <https://doi.org/10.1364/AO.41.002191>.
- Lee, Z., Carder, K.L., Hawes, S.K., Steward, R.G., Peacock, T.G., Davis, C.O., 1994. Model for the interpretation of hyperspectral remote-sensing reflectance. *Appl. Opt.* 33, 5721–5732. <https://doi.org/10.1364/ao.33.005721>.
- Lee, Z., Carder, K.L., Mobley, C.D., Steward, R.G., Patch, J.S., 1998. Hyperspectral remote sensing for shallow waters. I. A semianalytical model. *Appl. Opt.* 37, 6329–6338. <https://doi.org/10.1364/AO.37.006329>.
- Lee, Z., Carder, K.L., Mobley, C.D., Steward, R.G., Patch, J.S., 1999. Hyperspectral remote sensing for shallow waters. 2. Deriving bottom depths and water properties by optimization. *Appl. Opt.* 38, 5721–5732. <https://doi.org/10.1364/AO.38.003831>.
- Lepper, P., 2005. *Manual on the Methodological Framework to Derive Environmental Quality Standards for Priority Substances in Accordance with Article 16 of the Water Framework Directive (2000/60/EC)*. Fraunhofer-Institute Molecular Biology and Applied Ecology, Schnallenberg, Germany.
- Li, R.R., Kaufman, Y.J., Gao, B.C., Davis, C.O., 2003. Remote sensing of suspended

- sediments and shallow coastal waters. *IEEE Trans. Geosci. Remote Sens.* 41, 559–566. <https://doi.org/10.1109/TGRS.2003.810227>.
- Li, J., Yu, Q., Tian, Y.Q., Becker, B.L., 2017. Remote sensing estimation of colored dissolved organic matter (CDOM) in optically shallow waters. *ISPRS J. Photogramm. Remote Sens.* 128, 98–110. <https://doi.org/10.1016/j.isprsjprs.2017.03.015>.
- Liu, Y., Islam, A., Gao, J., 2003. Quantification of shallow water quality parameters by means of remote sensing. *Prog. Phys. Geogr.* 2, 24–43. <https://doi.org/10.1191/030913303pp357ra>.
- Louchard, E.M., Reid, R.P., Stephens, F.C., Davis, C.O., Leathers, R.A., T. Valerie, D., 2003. Optical remote sensing of benthic habitats and bathymetry in coastal environments at Lee Stocking Island, Bahamas: a comparative spectral classification approach. *Limnol. Oceanogr.* 48, Part 2, 511–521. doi:https://doi.org/10.4319/lo.2003.48.1.part_2.0511.
- Ma, Z., Ysebaert, T., van der Wal, D., Herman, P.M.J., 2018. Conditional effects of tides and waves on short-term marsh sedimentation dynamics. *Earth Surf. Process. Landf.* 43, 2243–2255. *Landforms*. <https://doi.org/10.1002/esp.4357>.
- Majozzi, N.P., Salama, M.S., Bernard, S., Harper, D.M., Habte, M.G., 2014. Remote sensing of euphotic depth in shallow tropical inland waters of Lake Naivasha using MERIS data. *Remote Sens. Environ.* 148, 178–189. <https://doi.org/10.1016/j.rse.2014.03.025>.
- Maritorena, S., Morel, A., Gentili, B., 1994. Diffuse reflectance of oceanic shallow waters: influence of water depth and bottom albedo. *Limnol. Oceanogr.* 39, 1689–1703.
- Marmot, M., Bell, R., 2018. SDGs: the sustainable development goals and health equity. *Epidemiology* 29, 5–7. <https://doi.org/10.1097/EDE.0000000000000773>.
- Martinez-Carranza, J., Calway, A., 2012. Remote sensing of bathymetry: an investigation into the effect of bottom reflectance on passive upwelling spectral irradiance. *Remote Sens. Environ.* 93, 493–510.
- Matthews, M.W., Bernard, S., Robertson, L., 2012. An algorithm for detecting trophic status (chlorophyll-a), cyanobacterial-dominance, surface scums and floating vegetation in inland and coastal waters. *Remote Sens. Environ.* 124, 637–652. <https://doi.org/10.1016/j.rse.2012.05.032>.
- McKinna, W.I.L., Werdell, P.J., 2018. Approach for identifying optically shallow pixels when processing ocean-color imagery. *Opt. Express* 26, A915–A928. <https://doi.org/10.1364/OE.26.000A95>.
- Mgengel, V., Spitzer, R.J., 1991. Application of remote sensing data to mapping of shallow sea-floor near by Netherlands. *Int. J. Remote Sens.* 57, 473–479.
- Millennium Ecosystem Assessment, 2005. Millennium ecosystem assessment: research needs. In: *Ecosystems and Human Well-Being: Synthesis*. Island Press, pp. 257–258.
- Mishra, S., Mishra, D.R., 2012. Normalized difference chlorophyll index: a novel model for remote estimation of chlorophyll-a concentration in turbid productive waters. *Remote Sens. Environ.* 117, 394–406. <https://doi.org/10.1016/j.rse.2011.10.016>.
- Mobley, C.D., 2003. Effects of optically shallow bottoms on upwelling radiances: bidirectional reflectance distribution function effects. *Limnol. Oceanogr.* 48 (Part 2), 337–345. https://doi.org/10.4319/lo.2003.48.1_part_2.0337.
- Moore, G.F., Aiken, J., Lavender, S.J., 1999. The atmospheric correction of water colour and the quantitative retrieval of suspended particulate matter in Case II waters: application to MERIS. *Int. J. Remote Sens.* 20, 1713–1733. <https://doi.org/10.1080/014311699212434>.
- Morel, A., Gentili, B., 1993. Diffuse reflectance of oceanic waters. II Bidirectional aspects. *Appl. Opt.* 32, 6864–6879. <https://doi.org/10.1364/AO.32.006864>.
- Mumby, P.J., Green, E.P., Edwards, A.J., Clark, C.D., 1999. The cost-effectiveness of remote sensing for tropical coastal resources assessment and management. *J. Environ. Manag.* 55, 157–166. <https://doi.org/10.1006/jema.1998.0255>.
- Mumby, P.J., Skirving, W., Strong, A.E., Hardy, J.T., LeDrew, E.F., Hochberg, E.J., Stumpf, R.P., David, L.T., 2004. Remote sensing of coral reefs and their physical environment. *Mar. Pollut. Bull.* 48, 219–228. <https://doi.org/10.1016/j.marpolbul.2003.10.031>.
- Murdoch, T.J.T., Aronson, R.B., 1999. Scale-dependent spatial variability of coral assemblages along the Florida reef tract. *Coral Reefs* 18, 341–351. <https://doi.org/10.1007/s003380050210>.
- Odermat, D., Pomati, F., Pitarch, J., Carpenter, J., Kawka, M., Schaepman, M., Wüest, A., 2012. MERIS observations of phytoplankton blooms in a stratified eutrophic lake. *Remote Sens. Environ.* 126, 232–239. <https://doi.org/10.1016/j.rse.2012.08.031>.
- Ogden, J.C., Porter, J.W., Smith, N.P., Szmant, A.M., Jaap, W.C., Forcucci, D., 1994. A long-term interdisciplinary study of the Florida Keys seascapes. *Bull. Mar. Sci.* 54, 1059–1071.
- Palandro, D.A., Andréfouët, S., Hu, C., Hallock, P., Müller-Karger, F.E., Dustan, P., Callahan, M.K., Kranenburg, C., Beaver, C.R., 2008. Quantification of two decades of shallow-water coral reef habitat decline in the Florida Keys National Marine Sanctuary using Landsat data (1984–2002). *Remote Sens. Environ.* 112, 3388–3399. <https://doi.org/10.1016/j.rse.2008.02.015>.
- Pan, Y., Shen, F., Verhoef, W., 2017. An improved spectral optimization algorithm for atmospheric correction over turbid coastal waters: a case study from the Changjiang (Yangtze) estuary and the adjacent coast. *Remote Sens. Environ.* 191, 197–214. <https://doi.org/10.1016/j.rse.2017.01.013>.
- Pasterkamp, R., Woerd, H.J. van D., Peters, S.W.M., Eleveld, M.A., 2003. Validation of MERIS level 2 products in the North Sea: Dutch results for 2002–2003. In: *Proceedings of the MAVT Meeting*. 51. Spatial analysis & Decision Support, Institute for Environmental Studies, pp. 2–11. <https://doi.org/10.1080/22797254.2018.1457937>.
- Pattanaik, A., Sahu, K., Bhutiyani, M.R., 2015. Estimation of shallow water bathymetry using IRS-multipletspectral imagery of Odisha coast, India. *Aquatic Procedia*. 4, 173–18. doi:<https://doi.org/10.1016/j.aqpro.2015.02.024>.
- Philippart, C.J.M., Salama, M.S., Kromkamp, J.C., van der Woerd, H.J., Zuur, A.F., Cadée, G.C., 2013. Four decades of variability in turbidity in the western Wadden Sea as derived from corrected Secchi disk readings. *J. Sea Res.* 82, 67–79. <https://doi.org/10.1016/j.seares.2012.07.005>.
- Phinn, S., Roelfsema, C., Dekker, A., Brando, V., Anstee, J., 2008. Mapping seagrass species, cover and biomass in shallow waters: an assessment of satellite multi-spectral and airborne hyper-spectral imaging systems in Moreton Bay (Australia). *Remote Sens. Environ.* 112, 3413–3425. <https://doi.org/10.1016/j.rse.2007.09.017>.
- Pitarch, J., Volpe, G., Coella, S., Krasemann, H., Santolieri, R., 2016. Remote sensing of chlorophyll in the Baltic Sea at basin scale from 1997 to 2012 using merged multi-sensor data. *Ocean Sci.* 12, 379–389. <https://doi.org/10.5194/os-12-379-2016>.
- Pitarch, J., van der Woerd, H.J., Brewin, R.J.W., Zielinski, O., 2019. Optical properties of Forel-Ule water types deduced from 15 years of global satellite ocean color observations. *Remote Sens. Environ.* 231, 111249. <https://doi.org/10.1016/j.rse.2019.111249>.
- Postma, H., 1982. *Hydrography of the Wadden Sea: movements and properties of water and particulate matter*. Ecology of the Wadden Sea 1.
- Reuter, R., Badewien, T.H., Bartholom, Ä., Braun, A., Lübben, A., Rullkötter, J., 2009. A hydrographic time series station in the Wadden Sea (southern North Sea). *Ocean Dyn.* 59, 195–211. <https://doi.org/10.1007/s10236-009-0196-3>.
- Rijkswaterstaat, 2018. *Getijtafels voor Nederland* 2019. SDU Uitgevers, the Hague.
- Ritchie, J.C., Zimba, P.V., Everitt, J.H., 2003. Remote sensing techniques to assess water quality. *Photogramm. Eng. Remote Sens.* 69, 695–704. <https://doi.org/10.14358/PERS.69.6.695>.
- Ruddick, K.G., De Cauwer, V., Park, Y.-J., Moore, G.F., 2006. Seaborne measurements of near infrared water-leaving reflectance: the similarity spectrum for turbid waters. *Limnol. Oceanogr.* 51, 1167–1179. <https://doi.org/10.4319/lo.2006.51.2.1167>.
- Salama, M.S., Shen, F., 2010. Simultaneous atmospheric correction and quantification of suspended particulate matters from orbital and geostationary earth observation sensors. *Estuar. Coast. Shelf Sci.* 86, 499–51. doi:<https://doi.org/10.1016/j.ecss.2009.10.001>.
- Salama, M.S., Su, Z., 2010. Bayesian model for matching the radiometric measurements of aerospace and field ocean color sensors. *Sensors* 10, 7561–7575. <https://doi.org/10.3390/s100807561>.
- Salama, M.S., Verhoef, W., 2015. Two-stream remote sensing model for water quality mapping: 2SeaColour. *Remote Sens. Environ.* 157, 111–122. <https://doi.org/10.1016/j.rse.2014.07.022>.
- Salama, M.S., Su, Z., Mannaaerts, C.M., Verhoef, W., 2009. Deriving inherent optical properties and associated uncertainties for the Dutch inland waters during the Eagle Campaign. *Hydrology & Earth System Sciences Discussions* 6, 2075–2098. <https://doi.org/10.5194/hessd-6-2075-2009>.
- Salama, M.S., Radwan, M., van der Velde, R., 2012a. A hydro-optical model for deriving water quality variables from satellite images (HydroSat): a case study of the Nile River demonstrating the future Sentinel-2 capabilities. *Physics and Chemistry of the Earth. Parts A/B/C* 50, 224–232.
- Salama, M.S., van der Velde, R., van der Woerd, H.J., Kromkamp, J.C., Philippart, C.J.M., Joseph, aT, O'Neill, P.E., Lang, R.H., Gish, T., Werdell, P.J., Su, Z., 2012b. Technical note: calibration and validation of geophysical observation models. *Biogeosciences* 9, 2195–2201. <https://doi.org/10.5194/bg-9-2195-2012>.
- Sandidge, J.C., Holter, R.J., 1998. Coastal bathymetry from hyperspectral observations of water radiance. *Remote Sens. Environ.* 65, 341–352. [https://doi.org/10.1016/S0034-4257\(98\)00043-1](https://doi.org/10.1016/S0034-4257(98)00043-1).
- Saulquin, B., Fablet, R., Bourg, L., Mercier, G., d'Andon, O.F., 2016. MEETC2: ocean color atmospheric corrections in coastal complex waters using a Bayesian latent class model and potential for the incoming sentinel 3 - OLCI mission. *Remote Sens. Environ.* 172, 39–49. <https://doi.org/10.1016/j.rse.2015.10.035>.
- Schroeder, T., Behnert, I., Schaale, M., Fischer, J., Doerffer, R., 2007. Atmospheric correction algorithm for MERIS above case-2 waters. *Int. J. Remote Sens.* 28, 1469–1486. <https://doi.org/10.1080/01431160600962574>.
- Shen, F., Verhoef, W., 2010. Suppression of local haze variations in MERIS images over turbid coastal waters for retrieval of suspended sediment concentration. *Opt. Express* 18, 12653–12662. <https://doi.org/10.1364/OE.18.012653>.
- Siegel, D.A., Wang, M., Maritorena, S., Robinson, W., 2000. Atmospheric correction of satellite ocean color imagery: the black pixel assumption. *Appl. Opt.* 39, 3582–3591. <https://doi.org/10.1364/AO.39.003582>.
- Stumpf, R.P., Frayer, M.L., Durako, M.J., Brock, J.C., 2006. Variations in water clarity and bottom albedo in Florida bay from 1985 to 1997. *Estuaries* 22, 431. <https://doi.org/10.2307/1353209>.
- Tillmann, U., Hesse, K.-J., Colijn, F., 2000. Planktonic primary production in the German Wadden Sea. *J. Plankton Res.* 22, 1253–1276. <https://doi.org/10.1093/plankt/22.7.1253>.
- Toming, K., Kutser, T., Uiboupin, R., Arikas, A., Vahter, K., Paavel, B., 2017. Mapping water quality parameters with Sentinel-3 Ocean and Land Colour Instrument imagery in the Baltic Sea. *Remote Sens.* 9, 1070. <https://doi.org/10.3390/rs9101070>.
- UN: United Nations, Department of Economic and Social Affairs, Population Division, 2019. *World Population Prospects 2019: Highlights*.
- UNEP, 2006. Marine and coastal ecosystems and human well-being: a synthesis report based on the findings of the Millennium Ecosystem Assessment. *J. Bertrand Russell Arch.* <https://doi.org/10.1196/annals.1439.003>.
- van de Hulst, H.C., 1980. *Light Scattering by Small Particles*. Book. Dover Publications, Inc, New York, the United States of America.
- van der Wal, D., Wielemaker-van den Dool, A., Herman, P.M.J., 2010. Spatial synchrony in intertidal benthic algal biomass in temperate coastal and estuarine ecosystems. *Ecosystems* 13, 338–351. <https://doi.org/10.1007/s10021-010-9322-9>.
- van der Woerd, H.J., Pasterkamp, R., 2008. HYDROPT: a fast and flexible method to retrieve chlorophyll-a from multispectral satellite observations of optically complex coastal waters. *Remote Sens. Environ.* 112, 1795–1807. <https://doi.org/10.1016/j.rse.2007.09.001>.
- Verhoef, W., 1985. Earth observation modeling based on layer scattering matrices.

- Remote Sens. Environ. 17, 165–178. [https://doi.org/10.1016/0034-4257\(85\)90072-0](https://doi.org/10.1016/0034-4257(85)90072-0).
- Verhoef, W., Bach, H., 2003. Simulation of hyperspectral and directional radiance images using coupled biophysical and atmospheric radiative transfer models. *Remote Sens. Environ.* 87, 23–41. [https://doi.org/10.1016/S0034-4257\(03\)00143-3](https://doi.org/10.1016/S0034-4257(03)00143-3).
- Verhoef, W., Jia, L., Xiao, Q., Su, Z., 2007. Unified optical-thermal four-stream radiative transfer theory for homogeneous vegetation canopies. *IEEE Trans. Geosci. Remote Sens.* 45 (6), 1808–1822.
- Verhoef, W., van der Tol, C., Middleton, E.M., 2018. Hyperspectral radiative transfer modeling to explore the combined retrieval of biophysical parameters and canopy fluorescence from FLEX – Sentinel-3 tandem mission multi-sensor data. *Remote Sens. Environ.* 204, 942–963. <https://doi.org/10.1016/j.rse.2017.08.006>.
- Volpe, V., Silvestri, S., Marani, M., 2011. Remote sensing retrieval of suspended sediment concentration in shallow waters. *Remote Sens. Environ.* 115, 44–54. <https://doi.org/10.1016/j.rse.2010.07.013>.
- Voss, K.J., Mobley, C.D., Sundman, L.K., Ivey, J.E., Mazel, C.H., 2003. The spectral up-welling radiance distribution in optically shallow waters. *Limnol. Oceanogr.* 48 (Part 2), 364–373. https://doi.org/10.4319/lo.2003.48.1.part_2.0364.
- Vrieling, A., 2006. Satellite remote sensing for water erosion assessment: a review. *Catena* 65, 2–18. <https://doi.org/10.1016/j.catena.2005.10.005>.
- Wang, M., 2005. Estimation of ocean contribution at the MODIS near-infrared wavelengths along the east coast of the U.S.: two case studies. *Geophys. Res. Lett.* 32. <https://doi.org/10.1029/2005GL022917>.
- Wang, M., 2007. Remote sensing of the ocean contributions from ultraviolet to near-infrared using the shortwave infrared bands: simulations. *Appl. Opt.* 46, 1535–1547. <https://doi.org/10.1364/AO.46.001535>.
- Wang, M., Shi, W., 2007. The NIR-SWIR combined atmospheric correction approach for MODIS ocean color data processing. *Opt. Express* 15, 15722–15733. <https://doi.org/10.1364/OE.15.015722>.
- Wilson, G.W., Fischetti, T.R., 2010. *Coastline Population Trends in the United States: 1960 to 2008*. US Department of Commerce, Economics and Statistics Administration, US Census Bureau, Washington, DC.
- Yu, X., Salama, M.S., Shen, F., Verhoef, W., 2016a. Retrieval of the diffuse attenuation coefficient from GOCI images using the 2SeaColour model: a case study in the Yangtze estuary. *Remote Sens. Environ.* 175, 109–119. <https://doi.org/10.1016/j.rse.2015.12.053>.
- Yu, X., Shen, F., Liu, Y., 2016b. Light absorption properties of CDOM in the Changjiang (Yangtze) estuarine and coastal waters: an alternative approach for DOC estimation. *Estuar. Coast. Shelf Sci.* 181, 302–311. <https://doi.org/10.1016/j.ecss.2016.09.004>.
- Zhan, H., Lee, Z., Shi, P., Chen, C., Carder, K.L., 2003. Retrieval of water optical properties for optically deep waters using genetic algorithms. *IEEE Trans. Geosci. Remote Sens.* 41, 1123–1128. <https://doi.org/10.1109/TGRS.2003.813554>.
- Zhao, J., Barnes, B., Melo, N., English, D., Lapointe, B., Muller-Karger, F., Schaeffer, B., Hu, C., 2013. Assessment of satellite-derived diffuse attenuation coefficients and euphotic depths in south Florida coastal waters. *Remote Sens. Environ.* 131, 38–50. <https://doi.org/10.1016/j.rse.2012.12.009>.
- Zibordi, G., Berthon, J.F., Mélin, F., D'Alimonte, D., Kaitala, S., 2009. Validation of satellite ocean color primary products at optically complex coastal sites: northern Adriatic Sea, Northern Baltic Proper and Gulf of Finland. *Remote Sens. Environ.* 113, 2574–2591. <https://doi.org/10.1016/j.rse.2009.07.013>.
- Zibordi, G., Holben, B., Mélin, F., D'Alimonte, D., Berthon, J.-F., Slutsker, I., Giles, D., 2010. AERONET-OC: An overview. *Can. J. Remote. Sens.* 36, 488–497. <https://doi.org/10.5589/m10-073>.